**Supporting Information for**

# *Understanding and Breaking Scaling Relations in Single-Site Catalysis: Methane-to-Methanol Conversion by Fe(IV)=O*

Terry Z. H. Gani[1], and Heather J. Kulik[1,*]

[1]Department of Chemical Engineering, Massachusetts Institute of Technology, Cambridge, MA 02139, email: hjkulik@mit.edu

**Contents**

**Computational details for SI calculations**

All calculations in the SI were performed according to the same computational details as in Sec. 2b of the main text unless otherwise stated. All single-point energy calculations were performed on the same optimized geometries as in the main text. Validation of reported trends in Figs. S1 to S5 was performed on a subset of 55 minimal model scaffolds from **Set 1** (comprising all homoleptic minimal models with $NH_3$, $PH_3$, $OH_2$ and $SH_2$ ligands, see Fig. 2 and Table S1) and a subset of 10 functionalized N4Py scaffolds from **Set 2** (comprising subset 2a as in Fig. 2). Additional localized orbital analysis throughout the SI also made use of ORCA 4.0[1]-calculated wavefunctions, which used the all-electron relativistic ZORA-def2-TZVPP basis set[2-3] and the RIJCOSX approximation[4] to speed up evaluation of exact exchange (SARC/J auxiliary basis set[5]).

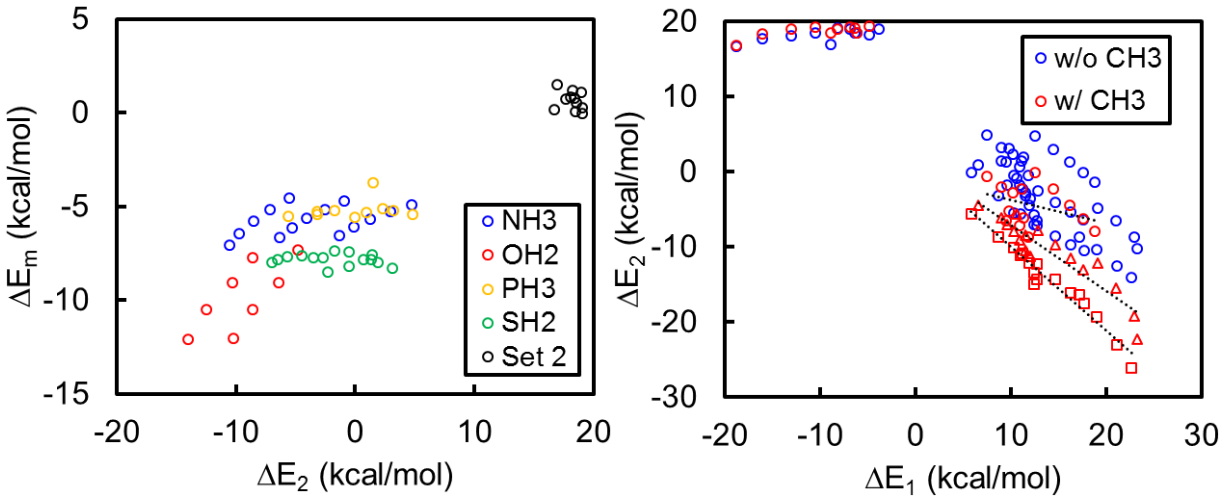


**Figure S1**. Effect of $CH_3^{\cdot}$ on reaction energetics. To justify omission of the antiferromagnetically (AFM) coupled methyl radical from our screening process, we optimized the AFM geometry for a subset of complexes (see Page S2 for details) and computed the binding energy of $CH_3^{\cdot}$ ($\Delta E_m$) as follows:

$$\Delta E_m = E(\mathbf{4}) - E(\mathbf{4a}) - E(CH_3^{\cdot}) \quad (1)$$

where each term is as defined in Fig. 1. Several complexes in the subset, namely those with $OH_2$ ligands and 10° dihedral angle, were discarded because the constrained optimization instead yielded the rebound alcohol product (**5**). In general, $\Delta E_m$ introduced additional connecting atom dependence, but otherwise does not affect overall trends. For the $NH_3$ and $OH_2$ minimal models, a strong dependence on bond length is noticed, with $\Delta E_m$ decreasing as the bond length is increased (left). As $\Delta E_2$ also decreases with as the bond length is increased, the underlying HAT trends remain unchanged, albeit with increased slope. This behavior appears to result from the Fe-O-H angle decreasing (i.e., becoming more acute) with bond length, and, interestingly, is confined to the $NH_3$ and $OH_2$ minimal models. This pathological behavior may suggest that they do not adequately represent "real" systems, but we have nevertheless retained them to adequately span the full range of octahedral ligand fields. In any case, this region of chemical space is likely inaccessible experimentally owing to poor stability and unfavorable oxo formation. For the subset of **Set 2** and the $PH_3$ and $SH_2$ containing minimal models, $\Delta E_m$ was found to be relatively constant across scaffolds with the same connecting atom. Across different connecting atoms, a general positive correlation between $\Delta E_m$ and $\Delta E_2$ exists. Hence, within the scatter inherent in our linear correlations, and noting that the anomalous behavior of $NH_3$ and $OH_2$ which is overrepresented here but does not extend to the rest of **Set 1**, the overall trends remain valid (see right subplot for illustration).

**Table S1**. Naming system for all complexes studied in this work. Cartesian coordinates of all optimized geometries are uploaded separately as xyz files. The 135 complexes that were discarded due to covalent bonding with the oxo moiety (see Sec. 3a) are not uploaded. These complexes primarily contain stretched Fe-P and Fe-S bonds, which undergo facile insertion of an oxygen atom to yield the corresponding O-coordinating ligand under the applied constraints. The file naming system for **Set 1** (minimal models) is `Fe-L1L2_n_i.xyz`, where L1 and L2 are the ligand identities as listed in Fig. 2 (Me = $CH_3$ and if L1 = L2, L2 is omitted), n represents the metal-ligand bond length-dihedral angle combination as tabulated below, and i = 1, 3, 4a, 5 represents the intermediate as in Fig. 1. The file naming system for **Set 2** is `2X_Y_i.xyz`, where X = a, b, c, d represents the positions that are functionalized (Fig. 2), Y represents the identity of the heavy atom (Fig. 2), and i = 1, 3, 4a, 5 represents the intermediate as in Fig. 1. Of the 40 scaffolds in **Set 2**, 3 were discarded (2d_I, 2d_P and 2d_S) due to covalent bonding between the oxo group and the heavy atom on the FG resulting from extreme steric repulsion.

| **n** | | **M-L BL (see Table S2)** | | | | |
|---|---|---|---|---|---|---|
| | | **1** | **2** | **3** | **4** | **5** |
| **Dihedral angle** | $10^o$ | 1 | 4 | 7 | 10 | 13 |
| | $20^o$ | 2 | 5 | 8 | 11 | 14 |
| | $30^o$ | 3 | 6 | 9 | 12 | 15 |

**Table S2**. Constrained geometry optimization details for **Set 1**. The constraints applied during geometry optimization of all intermediates are (1) the metal-ligand plane dihedral angle (i.e., 2-3-4-1 according to the atom numbering in the xyz files), which represents the degree of out-of-plane distortion of the metal atom that is extensively discussed in the main text, (2) the dihedral angle spanning the four coordinating atoms (i.e., 2-3-4-5 according to the atom numbering in the xyz files), which is always set to zero, and (3) each of the metal-ligand bond lengths. Each metal-connecting atom (i.e., N, O, P, S) pair is assigned one of five possible bond lengths (see Table S1 above) according to the table below (values in Å). These values were chosen such that an M-L BL value of **3** corresponds as closely as possible to the equilibrium quintet bond length. To illustrate our naming system, Fe-NH3OMe2_6 has Fe-N = 2.10 Å and Fe-O = 2.05 Å.

| **Connecting atom** | **M-L BL in Table S1** | | | | |
|---|---|---|---|---|---|
| | **1** | **2** | **3** | **4** | **5** |
| N | 2.00 | 2.10 | 2.20 | 2.30 | 2.40 |
| O | 1.95 | 2.05 | 2.15 | 2.25 | 2.35 |
| P | 2.50 | 2.60 | 2.70 | 2.80 | 2.90 |
| S | 2.40 | 2.50 | 2.60 | 2.70 | 2.80 |

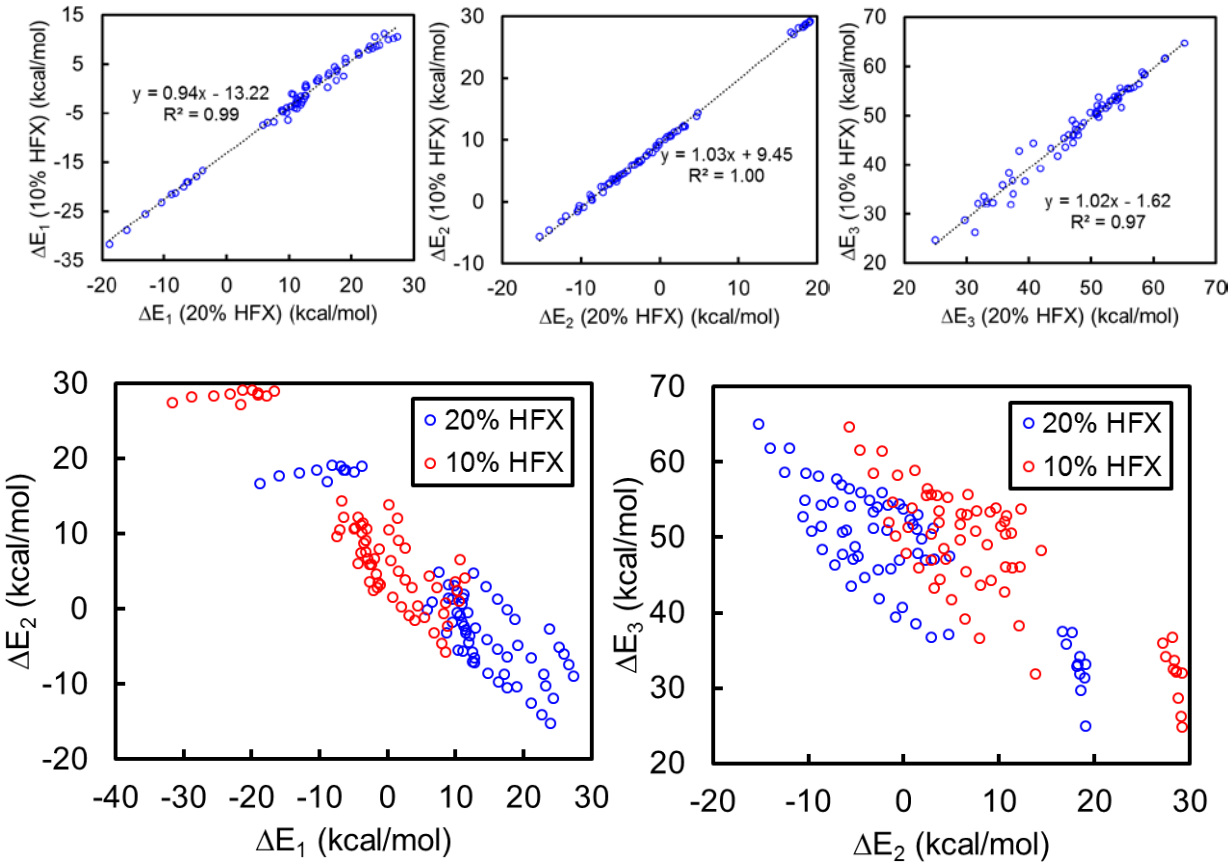


**Figure S2**. Functional sensitivity of reaction energetics. It is well-known that functional sensitivity in open-shell transition metal catalysts primarily stems from the fraction of Hartree-Fock exchange (HFX) used[6-8]. In a previous study of this catalytic cycle using a model catalyst, we found bond valence changes to be the primary driver of HFX sensitivity[8]. In this case, the formation of metal-ligand bonds causes oxo formation to be strongly favored by decreasing HFX, whereas the opposite is true for HAT. Hence, it might be expected that HFX sensitivity should be essentially constant across scaffolds, since the same bonds are broken and formed in each step. As a result, our trends should be invariant to functional choice. To confirm this, we recomputed single-point energies using a modified B3LYP with 10% HFX as in the TPSSh functional[6, 9] and compared the resulting reaction energies to those obtained from standard B3LYP (i.e., 20% HFX) (top subplots). Strong correlations with slopes of nearly 1 suggest that, as expected, all points are shifted by near-constant values. The correlations are excellent for $\Delta E_1$ and $\Delta E_2$. $\Delta E_3$ is generally insensitive to HFX but exhibits increased scatter, which may be due to varying degrees of covalency of the Fe-O interaction. Comparing overall correlations at each HFX value (bottom subplots) shows little impact on the underlying trends that are discussed in the main text.

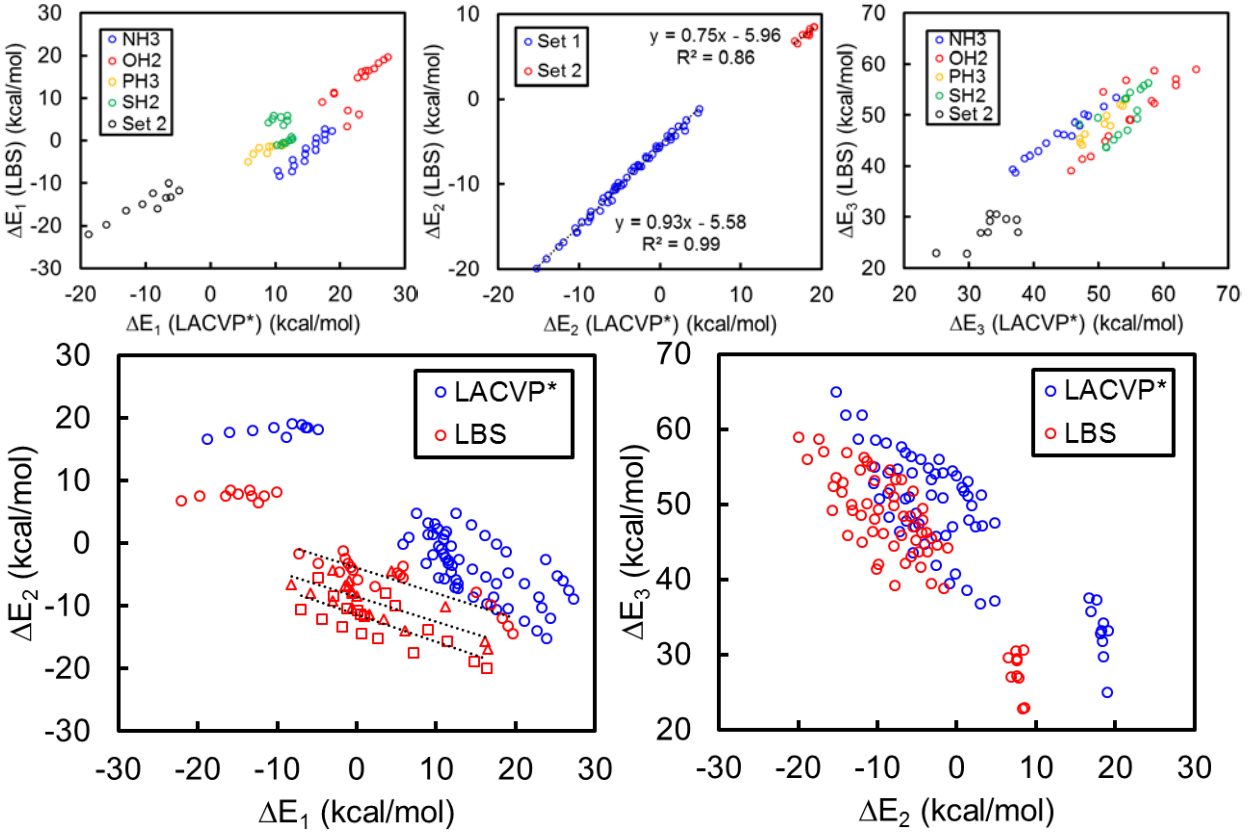


**Figure S3**. Basis set sensitivity of reaction energetics. To investigate the sensitivity of our reported energetics and trends to basis set choice, we computed reaction energetics with a larger basis set (LBS) using ORCA 4.0[1] (ZORA-def2-TZVPP, see Page S2 for details). The –I functionalized N4Py scaffold in **Set 2** was excluded as no comparable all-electron relativistic def2-TZVP basis set exists for I. On average, the use of the LBS favors both oxo formation and HAT. The best correlation is obtained for $\Delta E_2$, albeit with slightly different trends for **Sets 1** and **2**. Stronger system dependence is observed for $\Delta E_1$ and $\Delta E_2$, with the connecting atom identity affecting the degree to which the LBS favors oxo formation or $CH_3OH$ release, causing increased scatter in the resulting correlations. Nevertheless, the overall trends with respect to dihedral angle and ligand field strength still hold (bottom left, symbols represent different dihedral angles and have the same definition as in Fig. 3). The validity of trends with this LBS with reduced basis set superposition error (BSSE) also suggests that BSSE should not be a significant contribution when comparing trends among complexes.

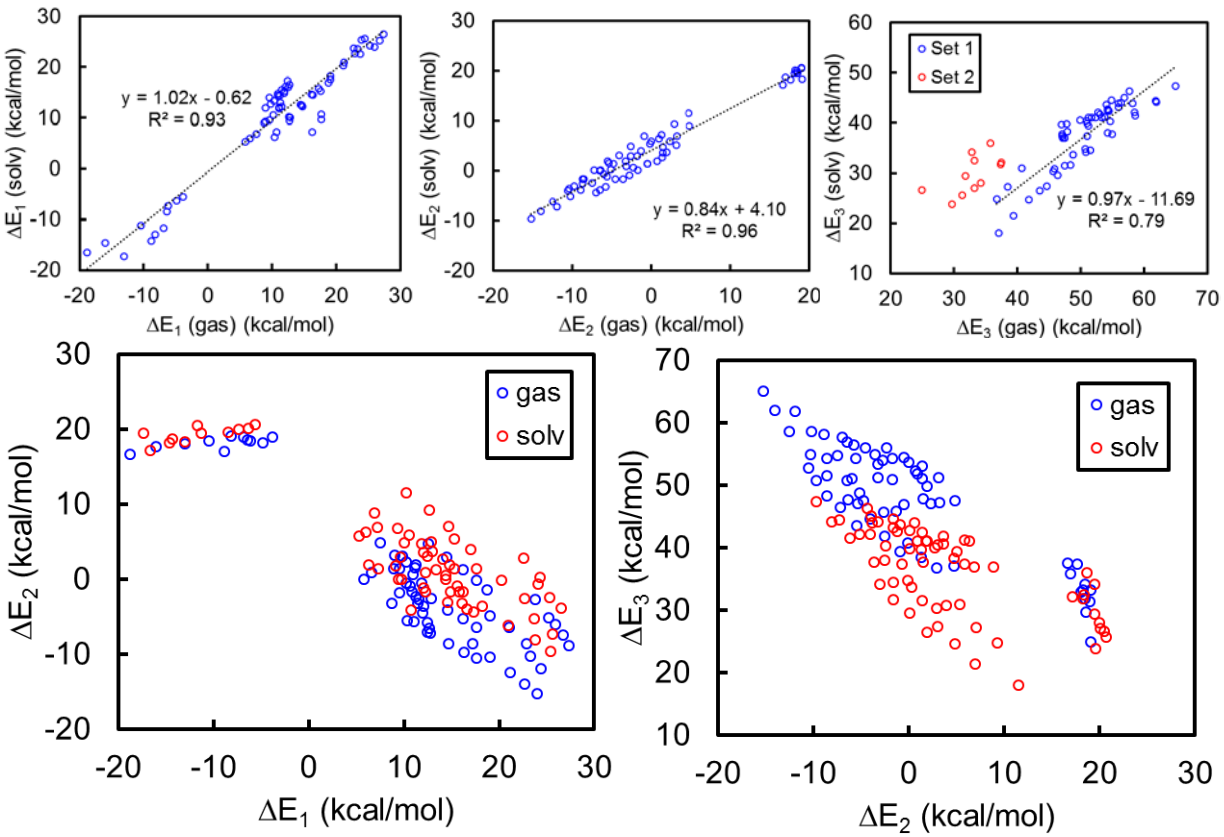


**Figure S4**. Effect of implicit solvent on reaction energetics. To investigate the effect of implicit solvent on reported energetics and trends, we recomputed reaction energetics including solvation energy contributions from the COSMO polarizable continuum model[10-11] as implemented in TeraChem using acetonitrile as solvent (ε = 37.5). This solvent is widely used in experimental studies of synthetic nonheme Fe(IV)-oxo intermediates (see, for instance, refs [12-13]), but we should also note that previous demonstrations of light alkane partial oxidation through this catalytic cycle have occurred in the gas phase[14-15]. The solute cavity was built using Bondi's van der Waals radii[16] scaled by a factor of 1.2 for available elements and a custom radius of 2.05 Å for Fe. Inclusion of implicit solvent affects $\Delta E_3$ most strongly as the release of $CH_3OH$ greatly increases the surface area for stabilizing solvent interactions, and this effect is more muted for **Set 2** compared to **Set 1** due to the larger scaffold size. However, scatter is also increased because of variations in the cavity shape and size with bond length and dihedral angle. These additional geometry-dependent effects worsen the correlations discussed in the main text, but the underlying electronic trends are still valid.

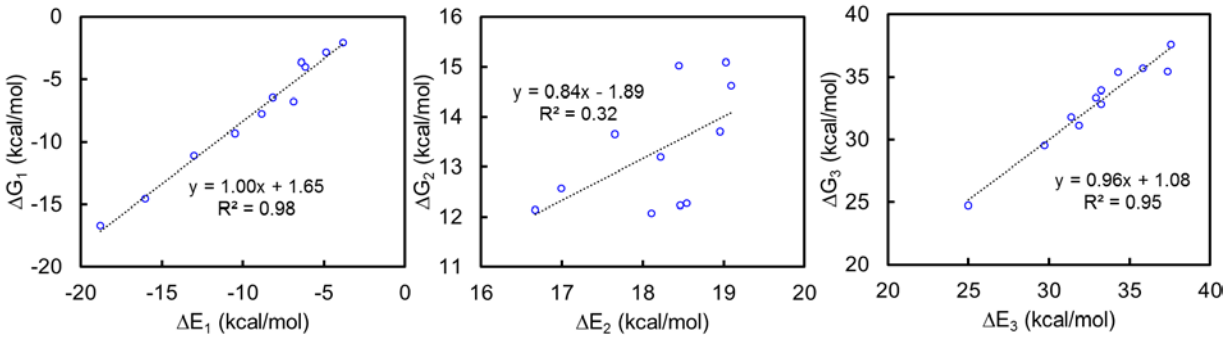


**Figure S5**. Effect of zero point vibrational energy (ZPVE) and entropic contributions to reaction energetics. To investigate the effect of ZPVE and entropic contributions on reported energetics and trends for **Set 2**, we performed numerical Hessian calculations in TeraChem on a subset (see Page S2) and computed these contributions under the harmonic approximation (T = 300 K), considering only vibrational contributions as follows:

$$G_{vib} = E + \mathrm{ZPVE} + E_{vib} - TS_{vib} \tag{2}$$

Translational and rotational contributions may trivially be computed but have been omitted as they are ill-defined for scaffolds that are heterogenized in some way (e.g., in porous frameworks[14] or covalently bound to an interface[17-18]). We observe (top) that vibrational contributions shift computed energies by 1-2 kcal/mol on average and add an additional 1-2 kcal/mol of uncertainty relative to electronic energies. The data for $\Delta E_2$ (center top) appear more scattered but only because there is little underlying variation (see Fig. 8). Hence, for **Set 2**, inclusion of vibrational contributions has no effect on overall trends.

As the constrained minimal models in **Set 1** are not stationary points, meaningful overall vibrational contributions cannot be computed. Hence, we instead investigate how the frequencies of the reactive Fe-O modes (i.e., Fe-O stretches in Fe(IV)-oxo, **2** and Fe(III)-hydroxo, **4a**) vary with connecting atom, metal-ligand bond length and dihedral angle, ignoring the spectator ligand-only modes which are unlikely to vary across scaffolds and the metal-connecting atom modes that lack physical meaning away from equilibrium. This approach is similar to that adopted in prior studies on metal-organic frameworks (MOFs)[19-20], in which constrained optimizations are physically justified by the structural rigidity of the porous crystalline structure. We find that, despite slight systematic frequency variations, the overall frequencies vary negligibly (i.e., within a ca. 100 $cm^{-1}$ range). (For comparison, an 800 $cm^{-1}$ mode such as the Fe-O single bond stretch in **4a** contributes about 1 kcal/mol to the ZPVE, 0.05 kcal/mol to $E_{vib}$ and 0.06 kcal/mol to $TS_{vib}$).

**Table S3**. Triplet-quintet splittings and two-state reactivity (TSR). It is well-known that TSR plays an important role in the reactivity of the Fe(IV)-oxo intermediate, with the quintet state being much more reactive than the triplet state owing to exchange-enhanced reactivity (EER), as discussed in the main text. Hence, it is desirable for the Fe(IV)-oxo species to have a quintet ground state, which is achievable with weak-field ligands as demonstrated in $Fe_2$(dobdc)[14]. Otherwise, spin-orbit coupling necessitates consideration of the spin-splitting energy as well as the triplet and quintet barriers, which has led to unexpected reactivity trends[21]. Here, we computed triplet-quintet splittings ($\Delta E$(HS-LS), kcal/mol = $E_{quintet} - E_{triplet}$) for representative substituted N4Py (**Set 2**) and minimal model (**Set 1**) complexes to evaluate the effect of substitutions and scaffold distortions respectively. We observe that N4Py substitutions have a limited effect on $\Delta E$(HS-LS) (i.e., a 3 kcal/mol range), whereas scaffold distortion has a much stronger effect, with a 40 kcal/mol difference between the strongest- and weakest-field scaffolds. This is in agreement with the locality of spin-state splittings[22] (i.e., the outsized impact of the immediate metal coordination environment).

It is thus instructive to compare reactivity trends with spin-splitting trends for the minimal model complexes. Firstly, we note that $\Delta E$(HS-LS) is governed by the difference in $d_{xy}/d_{x2-y2}$ energies (Fig. 4). Hence, although $d_{x2-y2}$ is nonbonding and does not affect quintet-state reactivity, it is nevertheless important in a TSR scenario. In addition to the effects described in Sec. 3a, increasing the ligand field strength at constant dihedral angle (e.g., by compressing the Fe-L bonds) also increases the $d_{xy}/d_{x2-y2}$ gap, thus disfavoring the quintet state (Fig. 4, right and Table S6). This places an additional constraint on ligand field tuning to favor HAT over oxo formation, as TSR will decrease HAT reactivity once the triplet state becomes the ground state. Scaffold distortion (i.e., increasing the dihedral angle) instead favors the quintet state (Fig. 4, left and Table S6), which is synergistic with the reactivity effects described in the main text.

| Scaffold | Modifier | ΔE(HS-LS) |
|---|---|---|
| 2a | Br | 9.2 |
| 2a | C | 10.6 |
| 2a | Cl | 10.0 |
| 2a | F | 10.7 |
| 2a | H | 12.9 |
| 2a | I | 9.6 |
| 2a | N | 11.4 |
| 2a | O | 12.7 |
| 2a | P | 11.5 |
| 2a | S | 11.1 |
| 2a | Si | 12.2 |

| | Fe-N bond length (Å) | | | | |
|---|---|---|---|---|---|
| **θ (deg)** | **2.0** | **2.1** | **2.2** | **2.3** | **2.4** |
| **10** | 22.0 | 9.2 | -0.7 | -8.4 | -14.2 |
| **20** | 17.5 | 5.4 | -3.6 | -11.0 | -16.4 |
| **30** | 11.6 | 0.4 | -8.5 | -14.1 | -19.1 |

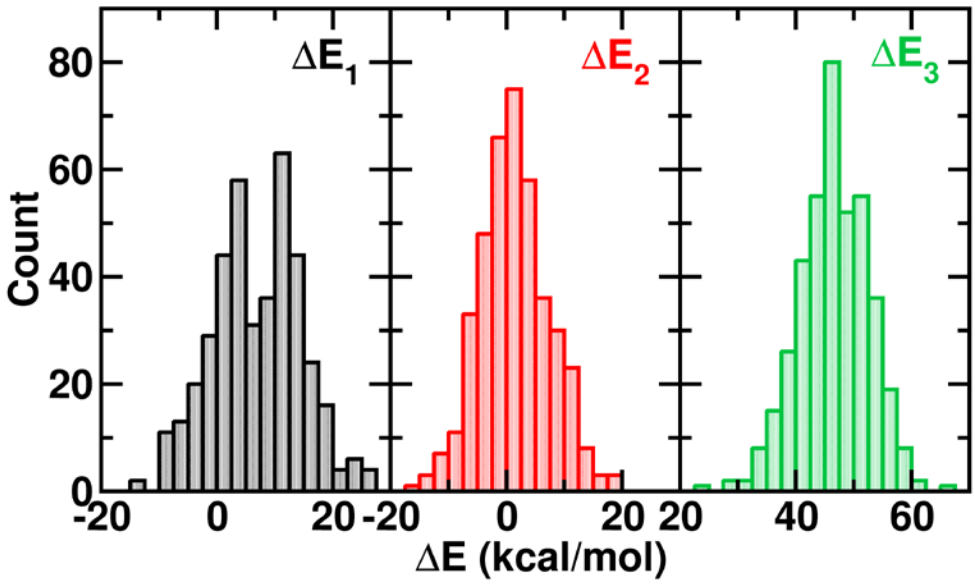


**Figure S6**. Histograms of $\Delta E_1$, $\Delta E_2$ and $\Delta E_3$ across **Set 1**. Note the wide ranges of ΔE and roughly normal distributions, with the comparable shapes suggesting moderate correlation.

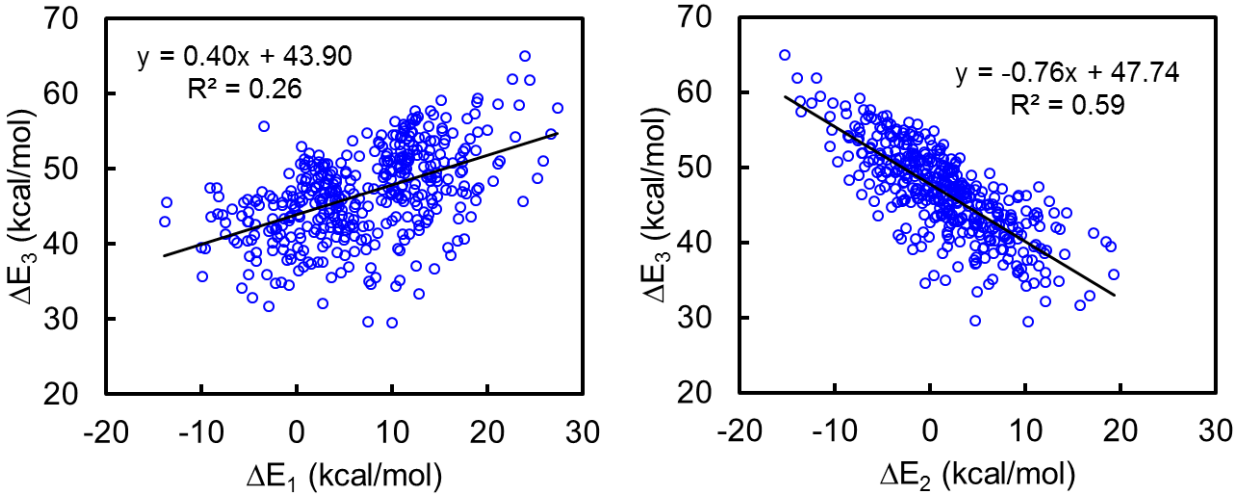


**Figure S7**. $\Delta E_3$ (kcal/mol) versus $\Delta E_1$ (kcal/mol) and $\Delta E_2$ (kcal/mol) for **Set 1** (outlier omitted – see main text). The significance of the strengths and signs of these correlations are discussed in the main text.

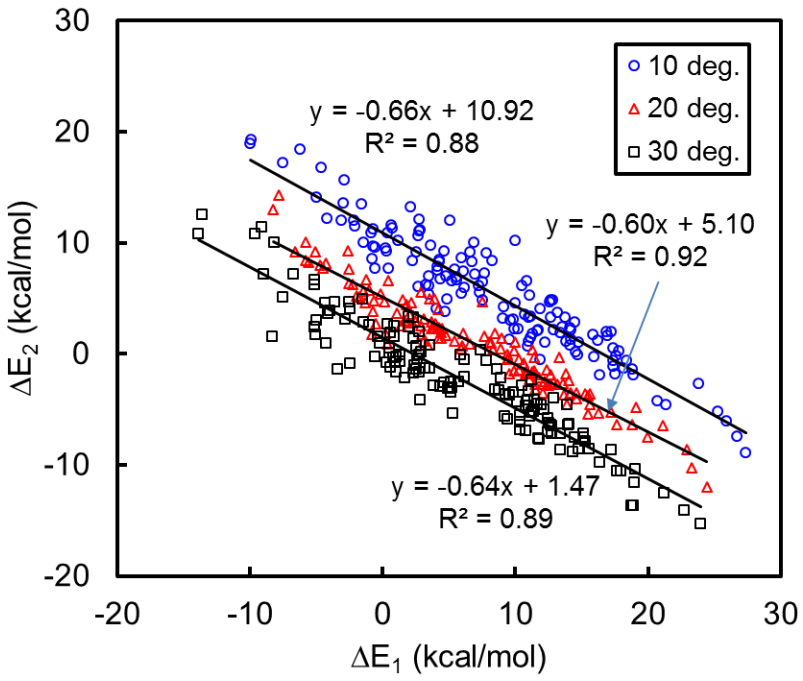


**Figure S8**. Linear fits for **Set 1** with constant dihedral angle (outlier omitted – see main text). Note the improved strength of these fits relative to **Set 1** as a whole, and the relatively constant slope as the dihedral angle is increased.

**Table S4**. Estimation of reaction energy sensitivity to dihedral angle. All energies are in units of kcal/mol, and sensitivities are in units of kcal/mol per ($10^o$ dihedral angle). To estimate overall sensitivities of $\Delta E_1$ and $\Delta E_2$, which we have assumed to be scaffold-independent and linear over the range of dihedral angles studied ($10^o$ to $30^o$), to the dihedral angle, we tabulated $\Delta E_1$ and $\Delta E_2$ at varying dihedral angles while holding the bond lengths (BL) constant (see Table S1 BL definitions), computed approximate sensitivities ($S(\Delta E_1)$ and $S(\Delta E_2)$) for each ligand-bond length pair using the finite difference approximation centered at $20^o$, and approximated the overall sensitivity as the arithmetic mean across all ligand-BL pairs. Pairs with missing data points (i.e., with scaffolds that were part of the 135 discarded) were not included.

| L1 | L2 | BL | ΔE1 | | | ΔE2 | | | S(ΔE1) | S(ΔE2) |
|---|---|---|---|---|---|---|---|---|---|---|
| | | | 10 deg. | 20 deg. | 30 deg. | 10 deg. | 20 deg. | 30 deg. | | |
| NH3 | NH3 | **1** | 12.6 | 10.6 | 10.4 | 4.7 | -0.9 | -5.5 | -1.10 | -5.12 |
| NH3 | OH2 | **1** | 16.9 | 9.9 | 11.0 | 2.0 | -1.6 | -4.6 | -2.95 | -3.31 |
| NH3 | OMe2 | **1** | 10.4 | 8.3 | 5.1 | 6.2 | 0.4 | -3.4 | -2.67 | -4.78 |
| NH3 | PH3 | **1** | 10.0 | 8.9 | 6.1 | 4.6 | 0.5 | -0.5 | -1.91 | -2.58 |
| NH3 | SH2 | **1** | 12.6 | 11.3 | 11.0 | 3.3 | 0.3 | -3.3 | -0.83 | -3.29 |
| NH3 | SMe2 | **1** | 2.5 | 2.2 | 2.5 | 9.2 | 4.6 | 0.7 | 0.01 | -4.26 |
| NMe3 | PH3 | **1** | 2.7 | -0.2 | -4.1 | 11.1 | 5.4 | 3.7 | -3.43 | -3.73 |
| NMe3 | SH2 | **1** | 5.1 | 2.9 | -1.5 | 12.0 | 5.6 | 5.0 | -3.30 | -3.54 |
| OH2 | OH2 | **1** | 23.8 | 19.1 | 17.2 | -2.6 | -4.8 | -8.6 | -3.27 | -3.00 |
| OH2 | OMe2 | **1** | 15.8 | 11.3 | 9.4 | 1.8 | -1.6 | -5.9 | -3.21 | -3.82 |
| OH2 | PH3 | **1** | 12.6 | 10.0 | 8.6 | 4.9 | 1.1 | -1.3 | -2.01 | -3.11 |
| OH2 | SH2 | **1** | 17.2 | 13.3 | 12.9 | 2.0 | -0.3 | -4.0 | -2.17 | -2.98 |
| OH2 | SMe2 | **1** | 6.7 | 3.9 | 1.9 | 8.3 | 4.9 | 3.4 | -2.39 | -2.47 |
| OMe2 | OMe2 | **1** | 10.8 | 7.6 | 4.9 | 6.6 | 1.6 | -3.1 | -2.96 | -4.83 |
| OMe2 | SMe2 | **1** | 2.7 | -5.8 | -2.6 | 10.7 | 8.4 | 4.7 | -2.63 | -2.97 |
| PH3 | PH3 | **1** | 7.5 | 6.6 | 5.8 | 4.8 | 0.9 | 0.0 | -0.84 | -2.44 |
| PH3 | PMe3 | **1** | -7.5 | -8.3 | -8.2 | 17.2 | 13.0 | 10.1 | -0.33 | -3.58 |
| PH3 | SH2 | **1** | 9.1 | 8.1 | 7.3 | 4.3 | 1.0 | 0.4 | -0.88 | -1.94 |
| PMe3 | SH2 | **1** | -6.3 | -7.8 | -9.1 | 18.5 | 14.3 | 11.4 | -1.43 | -3.52 |
| SH2 | SH2 | **1** | 9.8 | 9.0 | 11.2 | 3.1 | 1.4 | -2.3 | 0.71 | -2.70 |
| SMe2 | SMe2 | **1** | -3.0 | -5.6 | -6.7 | 13.6 | 8.2 | 7.2 | -1.89 | -3.22 |
| NH3 | NH3 | **2** | 14.5 | 12.8 | 12.7 | 2.9 | -2.6 | -7.2 | -0.87 | -5.05 |
| NH3 | NMe3 | **2** | 4.6 | 3.1 | 0.6 | 9.3 | 3.1 | -1.2 | -2.03 | -5.26 |
| NH3 | OH2 | **2** | 18.3 | 15.6 | 13.4 | -0.6 | -3.6 | -7.1 | -2.48 | -3.25 |
| NH3 | PH3 | **2** | 11.1 | 11.4 | 9.8 | 3.4 | -1.5 | -3.4 | -0.66 | -3.40 |
| NH3 | PMe3 | **2** | 0.7 | -2.5 | -4.3 | 11.4 | 7.6 | 4.6 | -2.51 | -3.39 |
| NH3 | SH2 | **2** | 13.3 | 12.3 | 11.6 | 2.0 | -1.4 | -4.5 | -0.87 | -3.22 |
| NH3 | SMe2 | **2** | 5.4 | 3.6 | 2.6 | 7.7 | 2.9 | -0.4 | -1.42 | -4.05 |
| NMe3 | NMe3 | **2** | 10.0 | 7.5 | 7.8 | 10.3 | 4.7 | -0.6 | -1.08 | -5.42 |
| NMe3 | OH2 | **2** | 8.2 | 3.6 | 1.0 | 8.4 | 5.0 | -0.2 | -3.62 | -4.32 |
| NMe3 | OMe2 | **2** | 3.6 | 0.1 | 0.2 | 9.8 | 4.7 | -0.7 | -1.67 | -5.28 |
| OH2 | OH2 | **2** | 25.2 | 21.1 | 19.0 | -5.1 | -6.5 | -10.3 | -3.10 | -2.61 |
| OH2 | OMe2 | **2** | 16.9 | 14.2 | 11.7 | 1.7 | -3.5 | -7.5 | -2.60 | -4.62 |
| OH2 | PH3 | **2** | 13.1 | 11.4 | 10.4 | 3.8 | -0.3 | -2.8 | -1.35 | -3.31 |
| OH2 | SH2 | **2** | 17.4 | 13.8 | 13.9 | 0.6 | -1.8 | -4.6 | -1.75 | -2.57 |
| OH2 | SMe2 | **2** | 6.9 | 4.1 | 2.3 | 7.2 | 4.0 | 3.3 | -2.31 | -1.95 |
| OMe2 | SH2 | **2** | 11.1 | 9.9 | 9.2 | 5.3 | 0.3 | -3.6 | -0.91 | -4.43 |
| OMe2 | SMe2 | **2** | 2.0 | 0.4 | -1.5 | 13.2 | 6.6 | 2.9 | -1.77 | -5.17 |
| Fe-PH3 | PH3 | **2** | 9.0 | 9.6 | 8.7 | 3.2 | -1.8 | -3.2 | -0.14 | -3.23 |
| PH3 | SH2 | **2** | 9.6 | 9.4 | 8.9 | 3.1 | -0.5 | -2.1 | -0.35 | -2.59 |
| PH3 | SMe2 | **2** | 2.7 | 1.3 | 0.9 | 6.1 | 2.6 | 1.6 | -0.90 | -2.28 |
| PMe3 | SMe2 | **2** | -5.0 | -6.6 | -9.0 | 14.1 | 9.2 | 7.2 | -2.00 | -3.47 |
| SH2 | SH2 | **2** | 11.3 | 10.3 | 11.9 | 1.9 | -0.5 | -4.5 | 0.32 | -3.20 |
| SH2 | SMe2 | **2** | 2.2 | 2.0 | 1.9 | 8.5 | 3.6 | 2.5 | -0.16 | -2.99 |
| SMe2 | SMe2 | **2** | -2.1 | -2.3 | -4.0 | 11.5 | 6.3 | 3.9 | -0.93 | -3.80 |
| NH3 | NH3 | **3** | 16.2 | 14.6 | 14.7 | 1.3 | -4.1 | -8.5 | -0.73 | -4.90 |
| NH3 | NMe3 | **3** | 6.0 | 4.4 | 4.3 | 7.5 | 2.0 | -2.9 | -0.87 | -5.21 |
| NH3 | OH2 | **3** | 18.9 | 17.2 | 15.5 | -1.9 | -5.3 | -8.6 | -1.67 | -3.34 |
| NH3 | OMe2 | **3** | 13.5 | 12.4 | 10.7 | 2.5 | -2.7 | -6.9 | -1.40 | -4.67 |
| NH3 | PH3 | **3** | 12.8 | 12.5 | 11.2 | 2.2 | -2.8 | -5.2 | -0.80 | -3.70 |
| NH3 | SH2 | **3** | 14.1 | 13.6 | 13.9 | 0.9 | -2.7 | -6.3 | -0.10 | -3.60 |
| NH3 | SMe2 | **3** | 5.2 | 3.9 | 0.9 | 6.6 | 2.3 | -0.7 | -2.14 | -3.61 |
| NMe3 | PH3 | **3** | 4.2 | 4.8 | 2.5 | 8.4 | 1.7 | -1.3 | -0.86 | -4.83 |
| NMe3 | SH2 | **3** | 5.9 | 4.0 | 5.7 | 8.7 | 2.7 | -2.5 | -0.13 | -5.58 |
| OH2 | OH2 | **3** | 25.9 | 22.9 | 21.2 | -6.0 | -8.6 | -12.5 | -2.38 | -3.24 |
| OH2 | OMe2 | **3** | 17.8 | 14.6 | 13.4 | 0.3 | -3.5 | -8.6 | -2.19 | -4.46 |
| OH2 | PH3 | **3** | 14.1 | 12.6 | 11.4 | 2.4 | -1.9 | -4.1 | -1.33 | -3.26 |
| OH2 | SH2 | **3** | 17.3 | 14.0 | 14.0 | -0.6 | -2.4 | -6.3 | -1.68 | -2.84 |
| OH2 | SMe2 | **3** | 6.1 | 2.2 | 2.7 | 6.0 | 2.8 | 2.0 | -1.70 | -1.97 |
| OMe2 | OMe2 | **3** | 13.8 | 10.6 | 9.2 | 3.3 | -0.8 | -5.6 | -2.30 | -4.46 |
| OMe2 | PH3 | **3** | 10.7 | 9.4 | 9.5 | 3.6 | -0.4 | -3.7 | -0.60 | -3.64 |
| OMe2 | SH2 | **3** | 11.0 | 11.3 | 10.8 | 3.4 | -1.7 | -4.6 | -0.12 | -4.00 |
| OMe2 | SMe2 | **3** | 0.3 | 1.8 | 0.6 | 10.9 | 4.4 | 2.0 | 0.13 | -4.48 |
| PH3 | SH2 | **3** | 9.9 | 10.3 | 10.9 | 2.3 | -1.4 | -4.1 | 0.50 | -3.20 |
| PH3 | SMe2 | **3** | 3.5 | 3.1 | 3.2 | 6.2 | 1.2 | -1.2 | -0.14 | -3.72 |
| PMe3 | PMe3 | **3** | -0.9 | -1.5 | -5.1 | 10.9 | 5.7 | 2.4 | -2.14 | -4.23 |
| SH2 | SH2 | **3** | 9.5 | 10.9 | 12.5 | 1.4 | -1.7 | -5.7 | 1.46 | -3.54 |
| SH2 | SMe2 | **3** | 3.4 | 2.9 | 2.3 | 7.0 | 2.5 | 1.4 | -0.57 | -2.80 |
| SMe2 | SMe2 | **3** | -1.5 | -1.3 | -1.0 | 10.0 | 4.6 | 2.7 | 0.25 | -3.68 |
| NH3 | NH3 | **4** | 17.6 | 16.2 | 16.3 | -0.1 | -5.3 | -9.7 | -0.63 | -4.78 |
| NH3 | NMe3 | **4** | 7.2 | 5.4 | 3.8 | 6.1 | 1.2 | -2.8 | -1.70 | -4.49 |
| NH3 | OH2 | **4** | 20.7 | 18.8 | 17.9 | -4.2 | -6.4 | -10.5 | -1.38 | -3.17 |
| NH3 | OMe2 | **4** | 14.7 | 13.9 | 11.8 | 1.0 | -4.5 | -7.6 | -1.48 | -4.34 |
| NH3 | PH3 | **4** | 13.8 | 13.7 | 12.6 | 1.2 | -3.6 | -6.3 | -0.60 | -3.75 |
| NH3 | SH2 | **4** | 14.7 | 14.1 | 14.5 | 0.0 | -3.6 | -7.5 | -0.11 | -3.73 |
| NH3 | SMe2 | **4** | 5.9 | 4.4 | 3.5 | 5.5 | 1.4 | -1.3 | -1.19 | -3.38 |
| NMe3 | OH2 | **4** | 7.5 | 3.7 | 2.7 | 6.5 | 2.3 | -1.6 | -2.38 | -4.03 |
| NMe3 | OMe2 | **4** | 4.1 | 1.9 | 1.0 | 7.9 | 2.8 | -1.6 | -1.55 | -4.76 |
| NMe3 | PH3 | **4** | 4.8 | 6.0 | 2.8 | 7.0 | 0.7 | -4.1 | -0.97 | -5.57 |
| NMe3 | SH2 | **4** | 5.6 | 4.5 | 5.1 | 6.9 | 2.3 | -2.4 | -0.21 | -4.69 |
| NMe3 | SMe2 | **4** | 0.4 | 0.2 | -3.4 | 7.8 | 1.8 | -1.3 | -1.92 | -4.55 |
| OH2 | OH2 | **4** | 26.7 | 23.3 | 22.7 | -7.4 | -10.2 | -14.0 | -2.01 | -3.29 |
| OH2 | OMe2 | **4** | 17.4 | 15.4 | 18.7 | -1.1 | -3.7 | -13.6 | 0.67 | -6.29 |
| OH2 | PH3 | **4** | 14.5 | 13.1 | 12.2 | 0.2 | -2.8 | -5.0 | -1.17 | -2.59 |
| OH2 | SH2 | **4** | 17.5 | 15.2 | 15.1 | -1.8 | -3.6 | -7.2 | -1.20 | -2.68 |
| OH2 | SMe2 | **4** | 4.1 | 4.1 | 2.9 | 7.5 | 2.4 | 0.2 | -0.61 | -3.66 |
| OMe2 | OMe2 | **4** | 14.2 | 11.5 | 10.3 | 2.2 | -1.8 | -6.1 | -1.95 | -4.11 |
| OMe2 | PH3 | **4** | 11.6 | 10.8 | 10.1 | 2.1 | -1.6 | -4.3 | -0.77 | -3.21 |
| OMe2 | SH2 | **4** | 11.7 | 11.8 | 11.2 | 2.2 | -2.1 | -5.3 | -0.27 | -3.71 |
| OMe2 | SMe2 | **4** | 0.3 | 2.5 | 0.5 | 9.2 | 3.0 | 0.6 | 0.12 | -4.34 |
| PH3 | PH3 | **4** | 11.1 | 11.5 | 11.0 | 1.5 | -3.2 | -5.6 | -0.03 | -3.53 |
| PH3 | SH2 | **4** | 10.9 | 11.0 | 11.3 | 1.1 | -2.3 | -5.1 | 0.20 | -3.13 |
| PH3 | SMe2 | **4** | 4.9 | 1.6 | 0.8 | 4.9 | 3.0 | -0.3 | -2.03 | -2.61 |
| PMe3 | PMe3 | **4** | 0.2 | -1.0 | -5.0 | 9.5 | 5.7 | 3.1 | -2.62 | -3.22 |
| SH2 | SH2 | **4** | 10.9 | 11.5 | 12.7 | 0.7 | -2.7 | -6.5 | 0.90 | -3.58 |
| SH2 | SMe2 | **4** | 3.4 | 3.0 | 1.2 | 5.4 | 1.8 | 0.0 | -1.09 | -2.71 |
| SMe2 | SMe2 | **4** | -0.8 | -0.7 | -0.4 | 8.6 | 3.9 | 1.6 | 0.21 | -3.51 |
| NH3 | NH3 | **5** | 18.8 | 17.6 | 17.6 | -1.3 | -6.4 | -10.5 | -0.57 | -4.59 |
| NH3 | NMe3 | **5** | 7.3 | 5.9 | 5.2 | 5.6 | 0.5 | -3.0 | -1.05 | -4.26 |
| NH3 | OH2 | **5** | 21.4 | 20.0 | 18.9 | -4.6 | -7.5 | -11.6 | -1.20 | -3.49 |
| NH3 | OMe2 | **5** | 15.9 | 15.5 | 14.3 | -0.2 | -5.4 | -8.8 | -0.79 | -4.32 |
| NMe3 | OH2 | **5** | 5.5 | 3.7 | 2.3 | 6.7 | 2.3 | -1.7 | -1.60 | -4.17 |
| NMe3 | OMe2 | **5** | 4.3 | -0.8 | 1.6 | 6.8 | 1.8 | -2.1 | -1.33 | -4.45 |
| OH2 | OH2 | **5** | 27.4 | 24.4 | 23.9 | -8.9 | -11.9 | -15.3 | -1.70 | -3.18 |
| OH2 | SH2 | **5** | 16.3 | 15.6 | 15.1 | -1.9 | -4.6 | -7.5 | -0.60 | -2.78 |
| OMe2 | OMe2 | **5** | 14.2 | 12.2 | 10.3 | 1.3 | -2.4 | -6.8 | -1.94 | -4.04 |
| OMe2 | SH2 | **5** | 12.2 | 12.1 | 12.5 | 1.1 | -2.7 | -6.2 | 0.14 | -3.64 |
| SH2 | SH2 | **5** | 11.8 | 12.1 | 12.4 | -0.5 | -3.5 | -7.0 | 0.30 | -3.25 |
| SH2 | SMe2 | **5** | 4.1 | 3.4 | 2.4 | 4.1 | 0.8 | -1.0 | -0.85 | -2.58 |
| SMe2 | SMe2 | **5** | -0.6 | -0.5 | -0.2 | 7.7 | 2.8 | 1.0 | 0.20 | -3.36 |

| | | |
|---|---|---|
| **AVERAGE** | **-1.2** | **-3.7** |
| **ST. DEV.** | **1.1** | **0.9** |

**Table S5**. Substituted methylated minimal models. To evaluate the extent of locality of inner-sphere effects, we generated minimal models in which a methyl H atom was substituted with another functional group as tabulated below (i.e., substitution three atoms away from the metal center). These structures all have Fe-N = 2.10 Å and 10° dihedral angle (i.e., **4** in Table S2). These distally substituted scaffolds generally behaved similarly to the unsubstituted scaffolds, confirming that there is little effect of functionalization beyond two atoms from the metal center.

| FG | E(1) (Ha) | E(3) (Ha) | E(4a) (Ha) | ΔE1 (kcal/mol) | ΔE2 (kcal/mol) |
|---|---|---|---|---|---|
| -NH2 | -876.251 | -951.398 | -952.057 | 8.8 | 13.4 |
| -C6H6 | -1051.978 | -1127.124 | -1127.783 | 8.9 | 13.6 |
| -Br | -833.444 | -908.587 | -909.247 | 10.6 | 12.9 |
| -Cl | -1280.482 | -1355.625 | -1356.286 | 10.3 | 12.9 |
| -F | -920.119 | -995.264 | -995.924 | 9.7 | 12.7 |
| -OH | -896.106 | -971.252 | -971.912 | 8.6 | 13.0 |
| -I | -831.663 | -906.808 | -907.468 | 9.9 | 12.6 |
| -PH2 | -1162.838 | -1237.980 | -1238.642 | 11.0 | 12.1 |
| -CCl3 | -2238.967 | -2314.110 | -2314.770 | 10.8 | 13.5 |
| -CF3 | -1157.921 | -1233.065 | -1233.724 | 10.2 | 13.2 |
| Unfunc. | -820.893 | -896.037 | -896.701 | 10.0 | 10.3 |

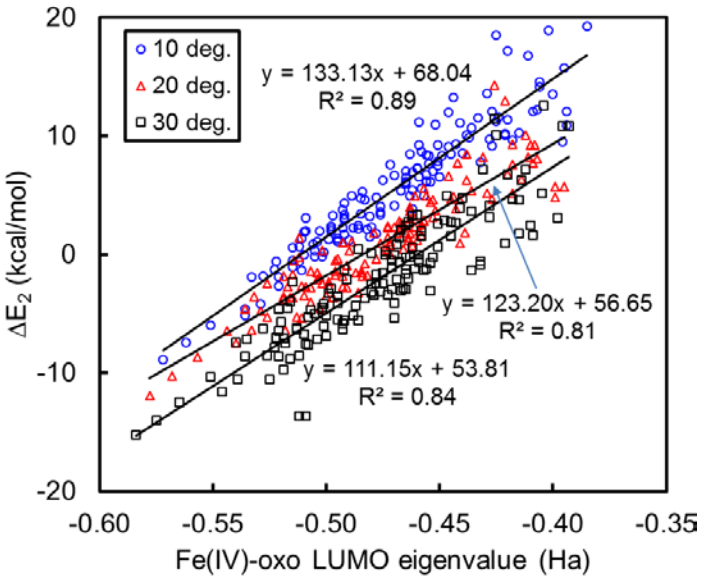


**Figure S9**. Illustration of the utility of the Fe(IV)-oxo LUMO eigenvalue as an electronic descriptor for HAT ($\Delta E_2$). As discussed in the main text, the high quality of the overall fit is consistent with previous studies. Nevertheless, there is still significant residual scatter that is attributable to variations in the $d_{xz}/d_{yz}$ eigenvalues which govern the strength of the breaking Fe=O π bond. When all *d* orbitals are shifted equally, as in ligand field tuning at constant dihedral angle, the eigenvalues of all *d* orbitals are well correlated and the $d_z^2$ LUMO eigenvalue remains a good single descriptor for HAT. However, structural distortion worsens its quality by decoupling $d_{xz}/d_{yz}$ and $d_z^2$ eigenvalues, which is mitigated by holding the dihedral angle constant.

**Table S6**. Representative DFT eigenvalue changes for Fe(II) (**1**) and Fe(IV)-oxo (**3**) upon metal-ligand bond stretching and out-of-plane distortion. The base, stretched and distorted complexes used here are Fe-NH3_7, Fe-NH3_13 and Fe-NH3_8 respectively (see Table S1 for naming system). All eigenvalues are reported in Ha and correspond to quasi-restricted orbitals[23] obtained with ORCA 4.0[1] (see Page S2) with the same orbital labeling as in Fig. 4. For doubly occupied orbitals (see Fig. 4), the average alpha and beta eigenvalues are reported.

| Fe(II) (**1**) | | | |
|---|---|---|---|
| Orbital(s) | Base | Stretched | Distorted |
| $d_{x^2-y^2}$ | -0.4598 | -0.5015 | -0.4639 |
| $d_{xz}/d_{yz}$ | -0.5585 | -0.5785 | -0.5541 |
| $d_{z^2}$ | -0.5700 | -0.5895 | -0.5692 |
| $d_{xy}$ | -0.6005 | -0.6229 | -0.6012 |
| Fe(IV)-oxo (**3**) | | | |
| Orbital(s) | Base | Stretched | Distorted |
| σ* | -0.4930 | -0.5081 | -0.5017 |
| $d_{x^2-y^2}$ | -0.5327 | -0.5658 | -0.5390 |
| π* | -0.5476 | -0.5576 | -0.5436 |
| $d_{xy}$ | -0.6021 | -0.6141 | -0.6044 |
| π | -0.6668 | -0.6819 | -0.6718 |
| σ | -0.7276 | -0.7366 | -0.7265 |

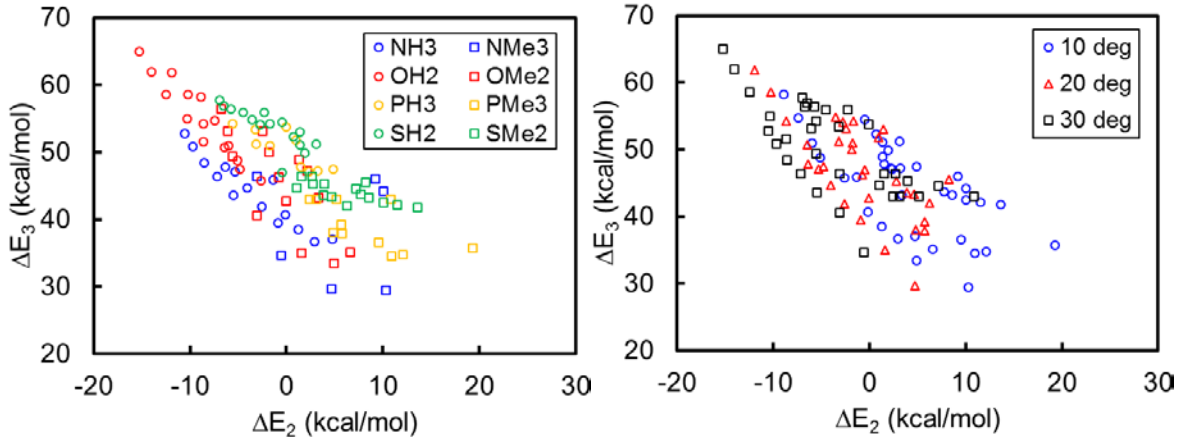


**Figure S10**. Property dependence of the $CH_3OH$ release energy. To illustrate the dependence of $\Delta E_3$ on multiple factors, we plotted $\Delta E_3$ against $\Delta E_2$ for selected homoleptic complexes as illustrated above. Trends with ligand identity held constant (i.e., with bond stretching or out-of-plane distortion) are relatively strong, but changing the ligand identity shifts points in a manner that cannot solely be attributed to the ligand field strength effect of the new ligand (left). We also note that fixing the dihedral angle does not improve correlations (right), and a weak size dependence may also arise from small differences in dispersion strengths.

**Table S7**. Minimal models used for HAT BEP analysis in Sec. 3b. The nomenclature is described in Table S1. In view of the high computational cost associated with nudged elastic band (NEB) TS searches (see Sec. 2b), TS energies were computed only for a subset of minimal models. To maximize diversity, we first removed all heteroleptic minimal models from what remained of **Set 1** after discarding the 135 scaffolds (see Table S1). Then, in view of the strong HAT exothermicity in many minimal models arising from undercoordination, which prevented TSs from being found in the minimal models with relatively weak ligand fields, we 1) performed the NEB calculations using a modified B3LYP at 10% HF exchange to increase the apparent HAT barriers without affecting trends (see discussion accompanying Fig. S2), and 2) discarded remaining minimal models where HAT TSs still could not be located. We note that the discarded structures are very unlikely to exhibit good catalytic performance because of the negative correlation between oxo formation and HAT and the rate-limiting nature of oxo formation. This procedure leaves 43 minimal models as tabulated below.

| **Ligand** | **M-L bond length combination** |
|---|---|
| NH3 | 1, 4, 7 |
| NMe3 | 5, 7, 10 |
| OMe2 | 1, 2, 4, 5, 7, 10, 13 |
| PH3 | 1, 4, 7, 10 |
| PMe3 | 1, 4, 6, 7, 8, 9, 10, 11, 12, 14 |
| SMe2 | 1, 2, 3, 4, 5, 6, 7, 8, 9, 10, 11, 12, 13, 14, 15 |

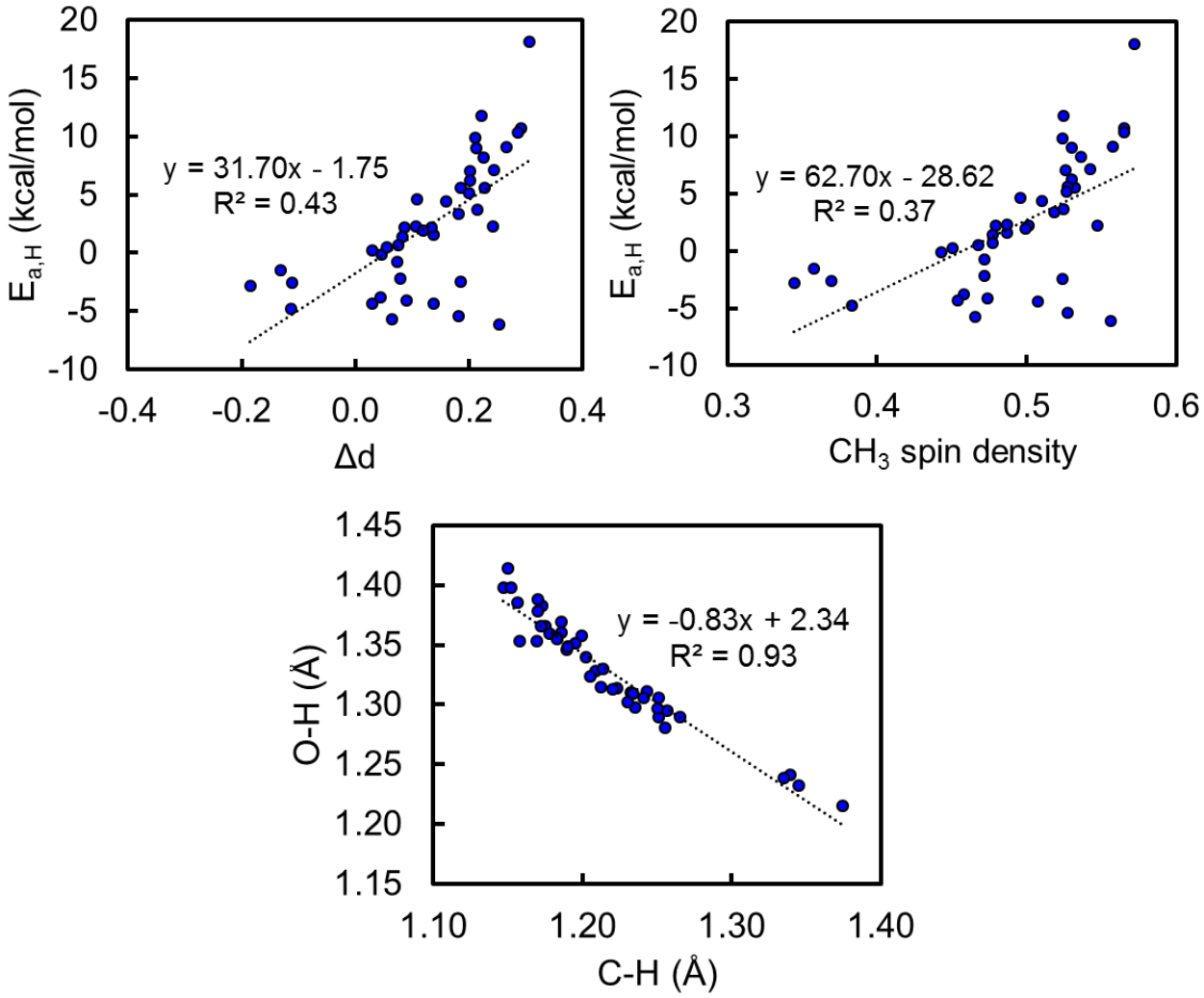


**Figure S11**. HAT activation energy vs. TS character. As discussed in the main text, the HAT reaction generally obeys the Hammond postulate, albeit with increased scatter for relatively late TSs that may be due to increased importance of variations in dispersion (left). To validate our metric of TS character, we also considered an alternative metric, namely the spin density of the incipient methyl group, which represents the degree of electron transfer to the complex (right). Both metrics yield qualitatively equivalent plots. We also correlated the forming O-H and cleaving C-H distances at the TS and obtained a good correlation (bottom), which is notable in comparison to the corresponding oxo formation correlation (Fig. S13).

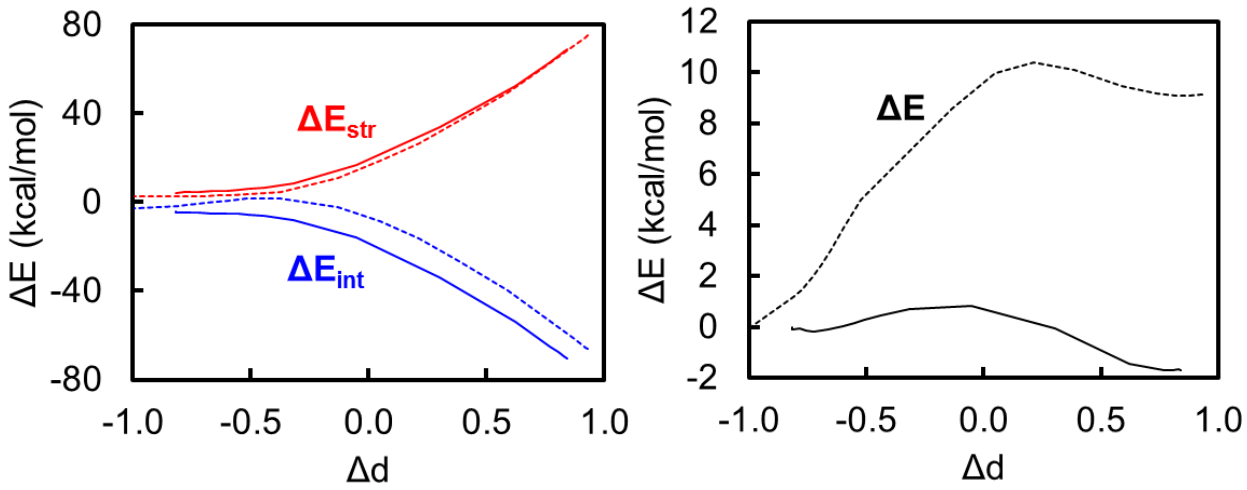


**Figure S12**. Activation strain analyses for HAT by representative low-barrier (OMe2_10, solid lines) and high-barrier (SMe2_1, dashed lines) minimal model complexes (see Table S1 for nomenclature). Owing to the divergent energy scales, the overall reaction energy profiles are plotted separately on the right. We recall that the activation strain model[24] (ASM) decomposes the relative energy (here $\Delta E_H$) at any point along a reaction coordinate into a strain component, $\Delta E_{str}$, corresponding to the energy required to deform the reacting fragments from their equilibrium geometry to their current geometry, and an interaction component, $\Delta E_{int}$, corresponding to the stabilization when the fragments interact at this geometry, i.e.:

$$\Delta E = \Delta E_{str} + \Delta E_{int} \tag{3}$$

where $\Delta E$ is obtained directly from the NEB path, $\Delta E_{str}$ is calculated from the single-point energies of isolated fragments, and $\Delta E_{int}$ is inferred. As in our previous work[8], we define the fragments as i) $CH_4$ and ii) the remainder of the complex, such that $\Delta E_{str}$ corresponds to Fe-O and C-H stretching and $\Delta E_{int}$ corresponds to O-H bond formation. $\Delta E_{int}$ is less favorable in the high-barrier complex owing to a weaker incipient O-H bond, which is only partially offset by a slight decrease in $\Delta E_{str}$ resulting from a slightly stronger Fe-O π bond (i.e., more favorable oxo formation). Past the TS, the magnitudes of these changes become almost independent of $\Delta d$, resulting in little change to the shape of the energy profile and explaining the observed slope.

**Table S8**. Minimal models used for oxo formation BEP analysis in Sec. 3b. The nomenclature is described in Table S1. As in HAT, TS energies were computed only for homoleptic minimal models, and owing to greater computational cost imposed by more difficult convergence, we further excluded the triply methylated $NMe_3$ and $PMe_3$ ligands. Unlike in HAT, the NEB calculations were performed with standard B3LYP as TSs could still be located even with high endothermicity. We further discarded 5 minimal models (PH3_3, SH2_2, SMe2_1, SMe2_2, SMe2_3) where the NEB algorithm failed to converge, leaving 76 minimal models as tabulated below.

| Ligand | M-L bond length combination |
|---|---|
| NH3 | 1-15 |
| OH2 | 1-12 |
| OMe2 | 1-5, 7-15 |
| PH3 | 1, 2, 4, 5, 6, 7, 10, 11, 12 |
| SH2 | 1, 3-15 |
| SMe2 | 4-15 |

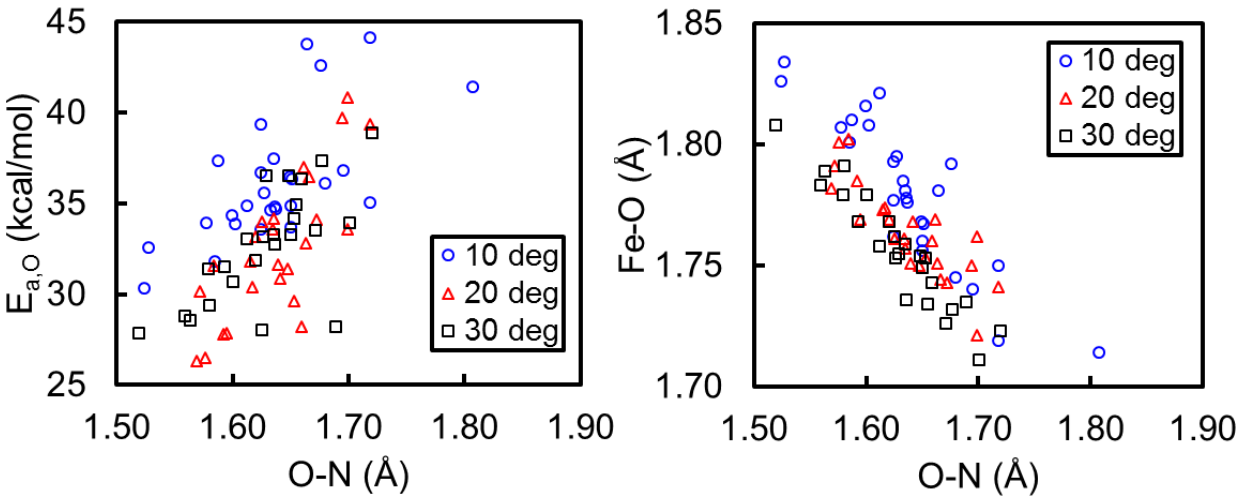


**Figure S13**. Oxo formation TS geometry correlations. We first note that the Hammond postulate is again obeyed, with later TSs, as measured by the bond length of the cleaving N-O bond, corresponding to higher barrier reactions (left). However, as discussed in the main text, plotting the forming Fe-O vs the cleaving O-N distances at the TS reveals dihedral angle dependence (right), whereas the corresponding correlation for HAT is much better (Fig. S11). This signifies that increasing the dihedral angle results in more favorable Fe-O bond formation early in the reaction coordinate that manifests as a stronger and shorter Fe-O bond at the TS, consistent with our electronic structure analysis in the main text.

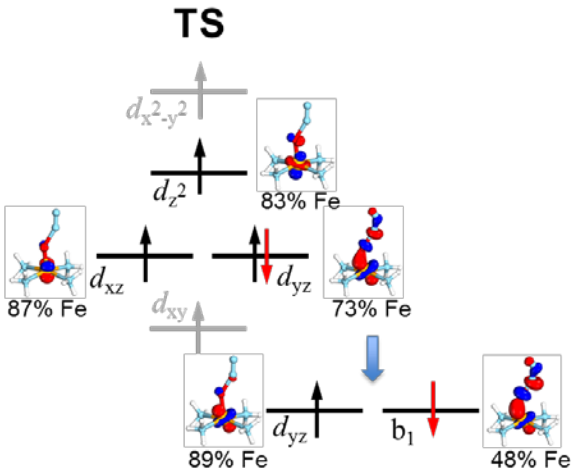


**Figure S14**. Localized orbital analysis for oxo formation. To justify our characterization of sequential electron transfer in the oxo formation reaction, we performed localized orbital analysis on the TS. Natural bond orbital (NBO) analysis[25] describes the TS as a high-spin Fe(III) complex with five spin-up lone pair electrons, which is confirmed by 1) quasi-restricted orbital (QRO) analysis[23] showing that the $d_z^2$ orbital remains occupied and localized on the metal center and 2) unrestricted corresponding orbital (UCO) analysis[26] showing that the doubly occupied $d_{xz}/d_{yz}$ orbital exhibits significant broken symmetry character (UCO overlap = 0.16), with the spin-down electron acquiring significant $N_2O$ character. The natural orbitals above are labeled with their Fe character. The spin-coupling is also consistent with an unrestricted B3LYP $\langle S^2 \rangle$ of about 6.3. We emphasize that the qualitative behavior observed here is entirely consistent with prior analysis on thioanisole sulfoxidation[27], which is an analogous reverse reaction. The QRO and UCO analysis was performed using ORCA 4.0[1] (Page S2) and orbital images were generated using IboView[28].

**Table S9**. Complexes with distal axial ligands added used to study oxo formation with full structural relaxation. We considered two sets of complexes here, one (left) with fixed axial ligand ($OH_2$) and varying equatorial ligands consisting of all possible combinations in Fig. 2 excluding $PH_3$ and $PMe_3$ owing to their tendency to covalently bond with the oxo moiety upon full structural relaxation, and another (right) with varying axial ligand and fixed equatorial ligands ($NH_3$).

| S/N | Ligand 1 | Ligand 2 | S/N | Ligand 1 | Ligand 2 |
|---|---|---|---|---|---|
| 1 | NH3 | NH3 | 10 | OH2 | OMe2 |
| 2 | NH3 | NMe3 | 11 | OH2 | SH2 |
| 3 | NH3 | OH2 | 12 | OH2 | SMe2 |
| 4 | NH3 | OMe2 | 13 | OMe2 | OMe2 |
| 5 | NH3 | SH2 | 14 | OMe2 | SH2 |
| 6 | NH3 | SMe2 | 15 | OMe2 | SMe2 |
| 7 | NMe3 | OH2 | 16 | SH2 | SH2 |
| 8 | NMe3 | OMe2 | 17 | SH2 | SMe2 |
| 9 | OH2 | OH2 | 18 | SMe2 | SMe2 |

| S/N | Axial ligand |
|---|---|
| 1 | MeCN |
| 2 | NH3 |
| 3 | NMe3 |
| 4 | OMe2 |
| 5 | PH3 |
| 6 | PMe3 |
| 7 | SH2 |
| 8 | SMe2 |

**Table S10**. Variations in metal-ligand bond lengths for oxo formation reacting complex (RC, **2** in Fig. 1), transition state (TS, **TS1**) and product complex (PC, **3**) in fully relaxed octahedral complexes. Although the metal-equatorial ligand bond lengths were kept frozen in minimal models, significant variations would otherwise exist along the reaction coordinate, which likely explain the observed increased scatter in BEP relations for unconstrained complexes relative to constrained minimal models. To illustrate this effect, we tabulated average metal- equatorial ligand (Fe-eq) and metal-axial ligand (Fe-ax) bond lengths for the unconstrained octahedral complexes with varying axial ligand identity. We do not observe clear trends along the reaction coordinate: Fe-eq is longer in the TS than the RC in some cases and shorter in others, and Fe-ax is longer in the PC than RC in some cases and shorter in others.

| | | **Bond lengths (Å)** | | | | | |
|---|---|---|---|---|---|---|---|
| | | Fe-eq | | | Fe-ax | | |
| **Eq lig** | **Ax lig** | **2** | **TS1** | **3** | **2** | **TS1** | **3** |
| NH3 | MeCN | 2.224 | 2.214 | 2.177 | 2.149 | 2.273 | 2.087 |
| NH3 | NH3 | 2.233 | 2.234 | 2.192 | 2.166 | 2.26 | 2.133 |
| NH3 | NMe3 | 2.231 | 2.234 | 2.14 | 2.196 | 2.296 | 2.232 |
| NH3 | OMe2 | 2.227 | 2.222 | 2.185 | 2.102 | 2.192 | 2.091 |
| NH3 | PH3 | 2.215 | 2.219 | 2.185 | 2.635 | 2.854 | 2.565 |
| NH3 | PMe3 | 2.224 | 2.234 | 2.184 | 2.547 | 2.674 | 2.527 |
| NH3 | SH2 | 2.21 | 2.209 | 2.184 | 2.626 | 2.88 | 2.559 |
| NH3 | SMe2 | 2.217 | 2.222 | 2.182 | 2.513 | 2.671 | 2.511 |

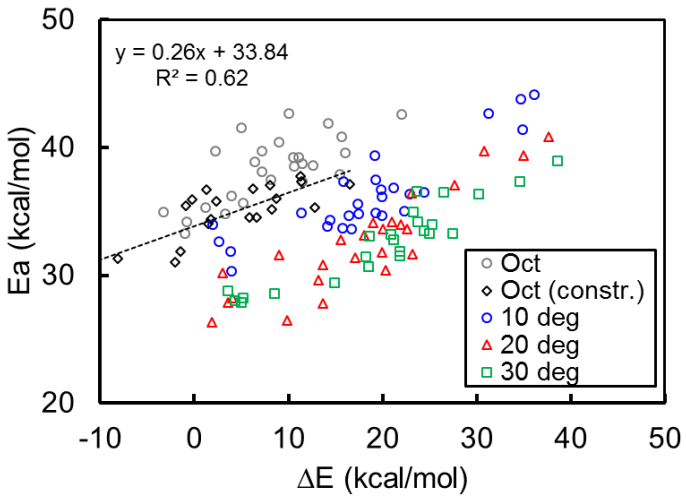


**Figure S15**. Comparison of constrained NEB and P-RFO for octahedral subset. To verify that the qualitative results of Fig. 5 (bottom) are independent of the TS search method, we recomputed reaction energies and barriers using the constrained NEB approach, where the equatorial ligands and Fe atom are fixed at their product (i.e., Fe(IV)-oxo) coordinates. As expected, the exclusion of the scaffold reorganization penalty through application of constraints lowers computed reaction energies slightly while also slightly reducing the scatter in the activation energies. Despite a slight downward shift in the activation energy vs. reaction energy plot, there is still a clear upward shift relative to the $10^{o}$ dihedral points (blue circles) with negligible change in slope (viz. best fit line equations in Fig. 5, bottom). Hence, our qualitative conclusions (i.e., that the intercept increases but the slope remains unchanged) remain valid.

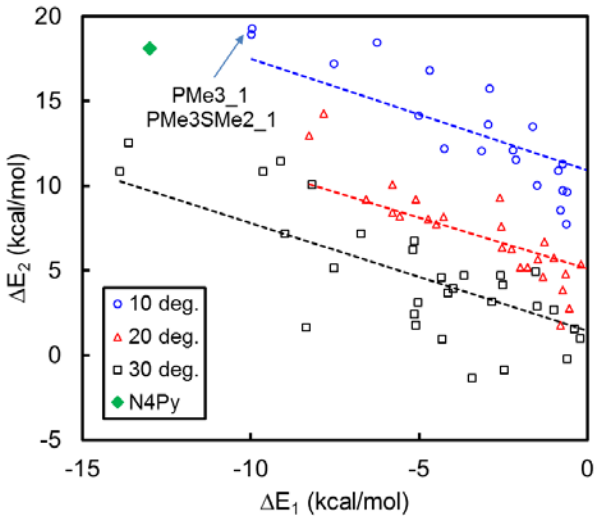


**Figure S16**. Analysis of N4Py energetics (larger green diamond) relative to minimal model energetics. This figure shows a close-up of Fig. S8 together with the N4Py point. We note that 1) the N4Py point lies within the region bounded by the 10º and 20º dihedral trendlines, and would similarly fall on a hypothetical trendline for 14º minimal minimal models within the inherent scatter, and 2) qualitatively, the nearest minimal model neighbors to the N4Py point are the strongest field minimal models, i.e., compressed $PMe_3$ and $SMe_2$.

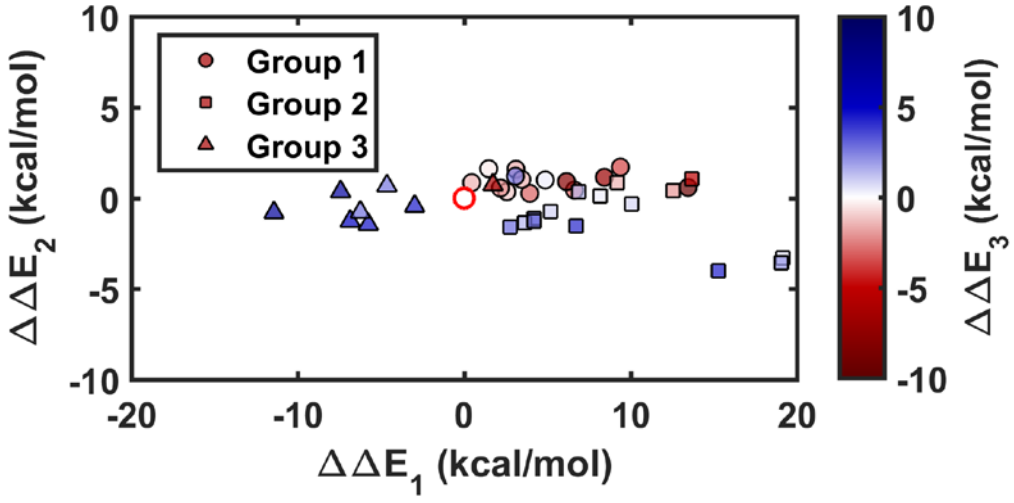


**Figure S17**. Additional correlation plot for **Set 2**. Here, we show how $\Delta\Delta E_2$ varies with $\Delta\Delta E_1$ across each of the groups discussed in the main text. $\Delta\Delta E_2$ here corresponds to the additional stabilization of the hydroxo group relative to the oxo group. Qualitatively, the low variability is consistent with the similar size, position and electronic properties of both moieties. Nevertheless, there are slight differences among groups, with Group II (i.e., steric interactions) generally increasing $\Delta E_2$ and Groups I and III (i.e., electrostatic interactions) generally decreasing $\Delta E_2$.

**Table S11**. Comparison of selected 3-substituted (i.e., distal) N4Py energetics with unsubstituted N4Py energetics. All energy changes are in units of kcal/mol. Here, we consider the 2d subset of **Set 2** to represent the worst-case quadruply-functionalized scenario. The distally substituted N4Py scaffolds share the same inner-sphere effects as the proximally substituted scaffolds discussed in the main text, among which we observe only narrow ranges of energetics compared to those in Figs. 8 and 9. This confirms that the second-sphere effects discussed in Sec. 3c are dominant over inner-sphere effects.

| **-R** | **E(1) (Ha)** | **E(2) (Ha)** | **E(4a) (Ha)** | **E(5) (Ha)** | **ΔE1** | **ΔE2** | **ΔE3** |
|---|---|---|---|---|---|---|---|
| Br | -1336.248 | -1411.429 | -1412.082 | -1452.023 | -13.0 | 18.0 | 35.8 |
| C | -1443.357 | -1518.540 | -1519.190 | -1559.129 | -13.8 | 19.0 | 33.8 |
| Cl | -3124.412 | -3199.592 | -3200.245 | -3240.186 | -12.6 | 18.0 | 35.5 |
| F | -1682.955 | -1758.135 | -1758.788 | -1798.729 | -12.5 | 17.9 | 35.6 |
| I | -1329.135 | -1404.316 | -1404.968 | -1444.908 | -13.0 | 18.3 | 34.9 |
| N | -1507.544 | -1582.729 | -1583.379 | -1623.312 | -15.4 | 19.7 | 31.4 |
| O | -1586.943 | -1662.126 | -1662.777 | -1702.714 | -14.0 | 19.0 | 33.3 |
| P | -2653.845 | -2729.027 | -2729.678 | -2769.616 | -13.6 | 18.8 | 34.0 |
| S | -2878.817 | -2954.000 | -2954.651 | -2994.588 | -13.9 | 18.9 | 33.7 |
| Si | -2448.848 | -2524.029 | -2524.681 | -2564.620 | -13.4 | 18.7 | 34.4 |
| H | -1286.039 | -1361.220 | -1361.872 | -1401.809 | -13.0 | 18.1 | 32.9 |
| | | | | **Range** | 2.8 | 1.8 | 4.4 |

**Table S12**. Electronic structure analysis of the Fe=O bond under noncovalent interactions (NCIs). One of the key fingerprints of electrostatic NCIs is their effect on the groups involved, in this case the Fe=O bond. If the oxo group is acting as a HB acceptor, we can expect a reduction in the Fe=O bond order, polarization of the Fe=O bond towards O and partial covalency of the O···H hydrogen bonding pair. Conversely, electrostatic repulsion of the oxo group should result in polarization of the Fe=O bond towards Fe, and steric repulsion should not affect the character of the Fe=O bond. Hence, to verify our characterization of NCIs, we analyzed how the Fe=O bond character, as determined by localized intrinsic bond orbital (IBO) analysis[29], performed in IboView[28], on large basis set-derived canonical orbitals (Page S2), changes with functionalization. Note that under this scheme, the bonding and antibonding majority-spin π orbitals cancel out, leaving two minority-spin bonding π orbitals as in the table below. The quantitative trends, notably the shift in relative atomic contributions to the Fe=O bond which represents the bond polarity, are in agreement with those expected of various NCIs as described above. The presence of hydrogen bonding in the –OH-substituted structure is consistent with (1) an increase in Fe-O bond length, and (2) the existence of (3,-1) bond critical points[30] between the O and H atoms, as computed by Multiwfn[31], under the atoms-in-molecules framework[32].

| **Orb.** | **Spin** | **2c, R = -OH** | | **N4Py** | | **2d, R = -SiH3** | | **2d, R = -Cl** | |
|---|---|---|---|---|---|---|---|---|---|
| | | % Fe | % O | % Fe | % O | % Fe | % O | % Fe | % O |
| σ | α | 39 | 60 | 43 | 57 | 41 | 59 | 59 | 40 |
| σ | β | 23 | 76 | 25 | 75 | 25 | 75 | 25 | 75 |
| π | β | 29 | 66 | 38 | 61 | 38 | 60 | 45 | 55 |
| π | β | 35 | 64 | 39 | 60 | 37 | 62 | 46 | 54 |
| | | Fe | O | Fe | O | Fe | O | Fe | O |
| Partial chg. | | 1.52 | -0.62 | 1.49 | -0.56 | 1.46 | -0.55 | 1.43 | -0.47 |
| Spin dens. | | 3.11 | 0.52 | 3.05 | 0.63 | 3.06 | 0.62 | 2.96 | 0.76 |
| Fe-O (Å) | | 1.63 | | 1.61 | | 1.61 | | 1.61 | |

**Table S13**. Relative energy changes attributable to second-sphere interactions in **Set 2**. All energy changes are in kcal/mol and as defined in Sec. 3c, and subsets are as defined in Fig. 2. Three points were omitted for reasons discussed in Table S1. Absolute energies are tabulated in the separately uploaded spreadsheet.

| Subset | FG | ΔΔE1 | ΔΔE2 | ΔΔE3 | Subset | FG | ΔΔE1 | ΔΔE2 | ΔΔE3 |
|---|---|---|---|---|---|---|---|---|---|
| Unfunc. | | 0.0 | 0.0 | 0.0 | | | | | |
| **2a** | C | 2.6 | 0.3 | -1.0 | **2b** | C | 0.5 | 0.8 | -1.5 |
| **2a** | P | 6.2 | 0.9 | -7.9 | **2b** | P | 3.5 | 1.0 | -1.5 |
| **2a** | S | 4.9 | 1.0 | 0.3 | **2b** | S | 2.2 | 0.6 | -2.2 |
| **2a** | Si | 6.6 | 0.4 | -3.2 | **2b** | Si | 4.0 | 0.3 | -3.1 |
| **2a** | F | 4.2 | -1.1 | 2.9 | **2b** | F | 2.8 | -1.6 | 3.0 |
| **2a** | Cl | 6.9 | 0.4 | 1.4 | **2b** | Cl | 3.6 | -1.4 | 1.4 |
| **2a** | Br | 8.2 | 0.1 | 0.4 | **2b** | Br | 4.2 | -1.3 | 2.8 |
| **2a** | I | 9.2 | 0.9 | -1.5 | **2b** | I | 5.2 | -0.7 | 0.9 |
| **2a** | N | -3.0 | -0.4 | 4.5 | **2b** | N | -4.7 | 0.7 | 2.7 |
| **2a** | O | -5.8 | -1.4 | 4.7 | **2b** | O | -6.2 | -0.8 | 2.8 |
| **2c** | C | 3.1 | 1.6 | -1.6 | **2d** | C | 1.5 | 1.6 | -0.4 |
| **2c** | P | 9.4 | 1.7 | -3.7 | | | | | |
| **2c** | S | 3.1 | 1.2 | 2.7 | | | | | |
| **2c** | Si | 8.4 | 1.1 | -7.0 | **2d** | Si | 13.5 | 0.6 | -9.5 |
| **2c** | F | 6.7 | -1.5 | 4.2 | **2d** | F | 15.3 | -4.0 | 4.4 |
| **2c** | Cl | 10.0 | -0.3 | 0.8 | **2d** | Cl | 19.2 | -3.3 | 0.7 |
| **2c** | Br | 12.6 | 0.4 | -2.1 | **2d** | Br | 19.1 | -3.6 | 2.0 |
| **2c** | I | 13.7 | 1.1 | -5.1 | | | | | |
| **2c** | N | -7.4 | 0.3 | 6.9 | **2d** | N | -6.8 | -1.3 | 5.2 |
| **2c** | O | -11.4 | -0.8 | 7.0 | **2d** | O | 1.7 | 0.7 | -6.4 |

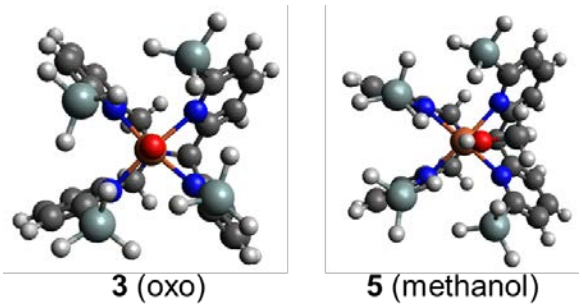


**Figure S18**. Analysis of geometric distortions to reduce steric repulsion. Here, we analyze optimized geometries to illustrate why steric repulsion has a greater destabilizing effect on oxo than methanol. Considering first the oxo-bound intermediate (left), the extent of steric repulsion is evident from the closest O-Si contact of only 81% of the sum of van der Waals (vdW) radii[16]. In this tetrafunctionalized scaffold, bulky groups surround the oxo group on all sides, such that distortion of the Fe=O bond will not help, and the axial N-Fe-O angle remains almost linear (176°). (In singly or doubly functionalized scaffolds, slight sideways distortion of the Fe=O bond is observed). The scaffold does attempt to distort to reduce these clashes by pulling the $SiH_3$ groups away from the active site, evident from the stretching of one Fe-N bond (top left) to 2.30 Å vs 2.13 Å in the unfunctionalized scaffold, but the rigidity of the scaffold limits the amount of distortion that can occur. The methanol in the methanol-bound intermediate (right) leverages the weaker Fe-O bond and asymmetry of the N4Py scaffold to distort sideways at a relatively low energetic cost (axial N-Fe-O angle = 160°). Coupled again with slight scaffold distortion, steric repulsion is greatly reduced as a result, with the closest O-Si contact now 91% of the sum of vdW radii.

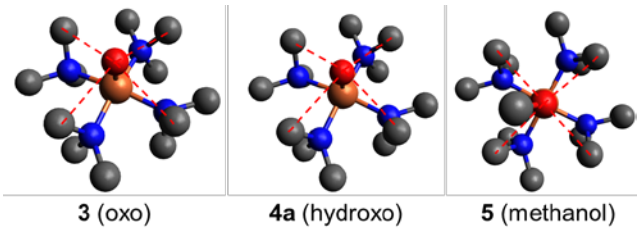


| | $(O\text{-}C)_{min,av}$ (Å) | Normalized |
|---|---|---|
| **3** | 2.74 | 0.85 |
| **4a** | 2.80 | 0.87 |
| **5** | 2.99 | 0.93 |

**Figure S19**. Structures of intermediates corresponding to the outlier point in Fig. 3. Hydrogen atoms have been removed for clarity and the red dashed lines indicate clashing atom pairs. The tabulated distances are the average closest O-C distance for each $NMe_3$ ligand, normalized by the sum of van der Waals radii of O and C (right). The combination of constrained short Fe-N distances and trimethylation forces steric clashes with at least one methyl group of each $NMe_3$ ligand, resulting in significant destabilization of bound moieties and deviation from the inner-sphere trendlines.

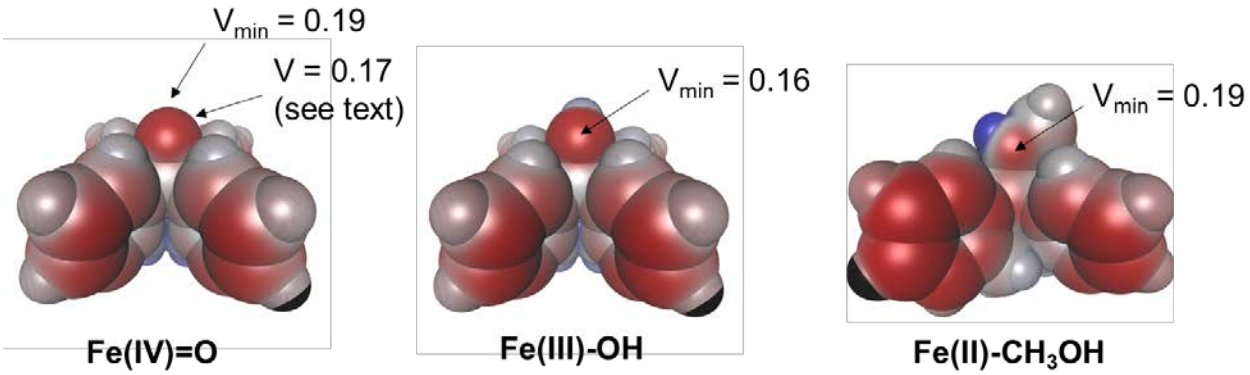


**Figure S20**. Comparison of hydrogen bond (HB) acceptor strengths. It is well-known that the magnitudes of ESP minima on a molecular surface, such as the van der Waals surface, are well-correlated to intrinsic HB acceptor strengths[33]. Hence, in order to predict relative HB acceptor strengths among metal-bound moieties (hydroxo, oxo, methanol), we computed the electrostatic potentials (ESPs) on van der Waals (vdW) surfaces of unsubstituted N4Py intermediates using QChem 4.4[34] and default settings. The color scale ranges from red (more electronegative, +0.2) to blue (less electronegative, +0.3), and the arrows indicate the locations of ESP minima. Here, all ESPs are positive owing to the net +2 charge of each complex and approach zero at infinite distance, but well-defined local minima still exist. The oxo moiety necessitates special discussion as the ESP minimum is at the top of the O atom as illustrated above, consistent with the orientation of the low-lying electron-accepting $d_z^2$ orbital, but the scaffold HB donors are constrained to form side-on HBs with the oxo moiety. Thus, it is the ESP value at that position that reflects the true HB acceptor strength of the oxo moiety. Furthermore, the top position has to be kept accessible in order for HAT via the low-energy $^5\sigma$ pathway to be facile. Using this adjusted ESP value for oxo, the ESP minima, on the vdW surface, and hence HB acceptor strength, follow the order hydroxo < oxo < methanol.

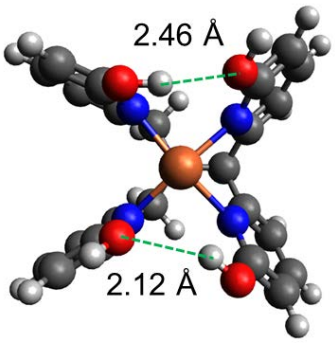


**Figure S21**. Illustration of intramolecular hydrogen bonding (green dashed lines) in the quadruply –OH functionalized N4Py scaffold of **Set 2**. This interaction stabilizes the unsaturated Fe(II) resting state (**1**) and hence shifts the corresponding point on Fig. 9 towards the bottom right.

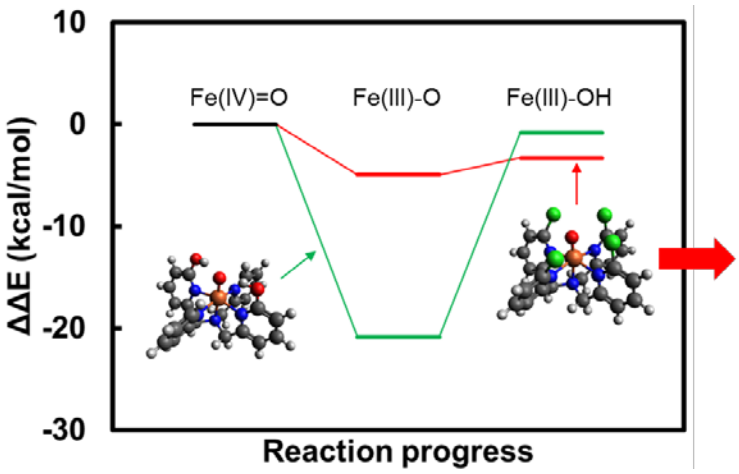


**Average distances (Å)**

| Atoms | Fe(IV)-oxo | Fe(III)-oxo |
|---|---|---|
| Fe-O | 1.61 | 1.68 |
| Fe-N | 2.15 | 2.32 |
| O-Cl | 3.02 | 3.20 |

**Figure S22**. Effect of noncovalent interactions (NCIs) on the relative stability of Fe(III)-oxo. Following the thermodynamic cycle approach to Fe(IV)-oxo reactivity[35], we first geometry optimized Fe(III)-oxo complexes for two representative functionalized scaffolds as illustrated above (+1 charge, sextet spin) and computed the energy difference between Fe(IV)-oxo to Fe(III)-oxo. The Fe(III)-hydroxo species is included for comparison. All energy differences are reported relative to the unfunctionalized scaffold. We see that the two HBs stabilize Fe(III)-oxo by about 20 kcal/mol relative to the unfunctionalized scaffold (left). Interestingly, the four repulsive $Cl^-$ groups also slightly stabilize Fe(III)-oxo because the increased Fe-N and Fe-O bond lengths reduce the distances between the O and Cl atoms (right).

**References:**


1. Neese, F. *Wiley Interdiscip. Rev.: Comput. Mol. Sci.* **2012,** *2*, 73-78.
2. Weigend, F.; Ahlrichs, R. *Phys. Chem. Chem. Phys.* **2005,** *7*, 3297-3305.
3. Van Wüllen, C. *J. Chem. Phys.* **1998,** *109*, 392-399.
4. Neese, F.; Wennmohs, F.; Hansen, A.; Becker, U. *Chem. Phys.* **2009,** *356*, 98-109.
5. Weigend, F. *Phys. Chem. Chem. Phys.* **2006,** *8*, 1057-1065.
6. Jensen, K. P. *Inorg. Chem.* **2008,** *47*, 10357-10365.
7. Simm, G. N.; Reiher, M. *J. Chem. Theory Comput.* **2016,** *12*, 2762-2773.
8. Gani, T. Z. H.; Kulik, H. J. *J. Chem. Theory Comput.* **2017,** *13*, 5443-5457.
9. Staroverov, V. N.; Scuseria, G. E.; Tao, J.; Perdew, J. P. *J. Chem. Phys.* **2003,** *119*, 12129-12137.
10. Klamt, A.; Schuurmann, G. *J. Chem. Soc., Perkin Trans. 2* **1993,** *2*, 799-805.
11. Liu, F.; Luehr, N.; Kulik, H. J.; Martínez, T. J. *J. Chem. Theory Comput.* **2015,** *11*, 3131-3144.
12. Sahu, S.; Widger, L. R.; Quesne, M. G.; De Visser, S. P.; Matsumura, H.; Moënne-Loccoz, P.; Siegler, M. A.; Goldberg, D. P. *J. Am. Chem. Soc.* **2013,** *135*, 10590-10593.
13. Widger, L. R.; Davies, C. G.; Yang, T.; Siegler, M. A.; Troeppner, O.; Jameson, G. N.; Ivanović-Burmazović, I.; Goldberg, D. P. *J. Am. Chem. Soc.* **2014,** *136*, 2699-2702.
14. Xiao, D. J.; Bloch, E. D.; Mason, J. A.; Queen, W. L.; Hudson, M. R.; Planas, N.; Borycz, J.; Dzubak, A. L.; Verma, P.; Lee, K. *Nat. Chem.* **2014,** *6*, 590-595.
15. Xiao, D. J.; Oktawiec, J.; Milner, P. J.; Long, J. R. *J. Am. Chem. Soc.* **2016,** *138*, 14371-14379.

16. Bondi, A. *J. Phys. Chem.* **1964,** *68*, 441-451.
17. Fukushima, T.; Drisdell, W.; Yano, J.; Surendranath, Y. *J. Am. Chem. Soc.* **2015,** *137*, 10926-10929.
18. Durkee, D. A.; Eitouni, H. B.; Gomez, E. D.; Ellsworth, M. W.; Bell, A. T.; Balsara, N. P. *Adv. Mater.* **2005,** *17*, 2003-2006.
19. Verma, P.; Vogiatzis, K. D.; Planas, N.; Borycz, J.; Xiao, D. J.; Long, J. R.; Gagliardi, L.; Truhlar, D. G. *J. Am. Chem. Soc.* **2015,** *137*, 5770-5781.
20. Liao, P.; Getman, R. B.; Snurr, R. Q. *ACS Appl. Mater. Interfaces* **2017,** *9*, 33484–33492.
21. Sastri, C. V.; Lee, J.; Oh, K.; Lee, Y. J.; Lee, J.; Jackson, T. A.; Ray, K.; Hirao, H.; Shin, W.; Halfen, J. A.; Kim, J.; Que Jr, L.; Shaik, S.; Nam, W. *Proc. Natl. Acad. Sci. U. S. A.* **2007,** *104*, 19181-19186.
22. Janet, J. P.; Kulik, H. J. *J. Phys. Chem. A* **2017,** *121*, 8939-8954.
23. Neese, F. *J. Am. Chem. Soc.* **2006,** *128*, 10213-10222.
24. van Zeist, W.-J.; Bickelhaupt, F. M. *Org. Biomol. Chem.* **2010,** *8*, 3118-3127.
25. Reed, A. E.; Weinstock, R. B.; Weinhold, F. *J. Chem. Phys.* **1985,** *83*, 735-746.
26. Neese, F. *J. Phys. Chem. Solids* **2004,** *65*, 781-785.
27. Wilson, S. A.; Chen, J.; Hong, S.; Lee, Y.-M.; Clémancey, M.; Garcia-Serres, R.; Nomura, T.; Ogura, T.; Latour, J.-M.; Hedman, B.; Hodgson, K. O.; Nam, W.; Solomon, E. I. *J. Am. Chem. Soc.* **2012,** *134*, 11791-11806.
28. Iboview -- a Program for Chemical Analysis. http://www.iboview.org/ (accessed August 31, 2017).
29. Knizia, G. *J. Chem. Theory Comput.* **2013,** *9*, 4834-4843.
30. Grabowski, S. J. *Chem. Rev.* **2011,** *111*, 2597-2625.
31. Lu, T.; Chen, F. *J. Comput. Chem.* **2012,** *33*, 580-592.
32. Bader, R. F. W., *Atoms in Molecules*. Wiley Online Library: 1990.
33. Hunter, C. A. *Angew. Chem. Int. Ed.* **2004,** *43*, 5310-5324.
34. Shao, Y.; Gan, Z.; Epifanovsky, E.; Gilbert, A. T.; Wormit, M.; Kussmann, J.; Lange, A. W.; Behn, A.; Deng, J.; Feng, X. *Mol. Phys.* **2015,** *113*, 184-215.
35. Borovik, A. S. *Chem. Soc. Rev.* **2011,** *40*, 1870-1874.